Tribology International 213 (2026) 111006

Contents lists available at ScienceDirect

Tribology International

journal homepage: www.elsevier.com/locate/triboint

Full Length Article

A variational method to wear with embedded roughness

Francis John [a], Pavan Kumar Asur Vijaya Kumar [b], Maria Rosaria Marulli [a,*], Marco Paggi [a]

[a] IMT School for Advanced Studies Lucca, Piazza San Francesco 19, 55100 Lucca, Italy
[b] Institute of Lightweight Design and Structural Biomechanics, Technische Universität Wien, Getreidemarkt 9, 1060 Vienna, Austria

ARTICLE INFO

Keywords:
Contact mechanics
Finite element method
Waviness
Roughness
Adhesive wear

ABSTRACT

A variational approach to contact mechanics with friction for the prediction of wear evolution under various indenters is proposed in this work. The contact problem is solved using the eMbedded Profile for Joint Roughness (MPJR) interface finite elements, here advanced to predict wear arising from the frictional contact problem between an indenter of any complex shape and an elastic body. The interface finite element formulation embeds the indenter shape, roughness, or any general deviation from planarity directly in the computation of the normal gap, updating the indenter geometry in time to account for the effect of wear through a microscopically postulated local Archard adhesive wear model. The formulation employs a regularized Coulomb law of friction to compute the tangential contact response, while a penalty approach is used to enforce the unilateral contact constraint. The methodology is exploited to get an insight into the complex relation between the macroscopically emergent global wear effects and the wear law at the microscale, which are intrinsically coupled through geometrical effects. To show the model predictive capability, the numerical examples consider three different indenter profiles with flat, cylindrical, and rough geometry.

1. Introduction

Wear is a consequence of the repetitive relative motion between two solids in contact. Consequently, wear leads to material loss, surface degradation, and decreased performance of mechanical components in time. Computational modeling of friction and wear is essential in engineering applications and poses several challenges due to the difficulties arising from tribology [1]. With the advent of computational methods and powerful tools such as the finite element method (FEM) and the boundary element method (BEM), physical and mechanical contact phenomena can be reconstructed with high precision. Reliable computational tools for predicting friction and wear are needed considering complex surface interactions from the microscale to the macroscale.

At the microscale, wear is influenced by factors such as surface roughness, material properties, and nonuniform contact pressure distributions. A micro-to-macro modeling approach aims to capture these microscale effects and their interaction which result into the emergent macroscale behavior of the component. This is achieved through modeling techniques, which simulate the wear process at both the micro and macro levels. Information derived from wear analysis can be used to optimize design and improve mechanical performance effectively, consequently extending the lifespan of mechanical systems.

Among the many different forms of wear, adhesive wear based on the well-known approach by Archard [2], assumes that wear is due to debris formation by asperity interlocking and fracture [3–5]. Analytical approaches can be found in [6–10], see [11] for an in-depth review of the field.

Literature regarding the numerical approximations of wear is abundant. Early numerical analyses of worn-out solids were given in [12–20]. In particular, the analyses in [14,15] looked at the evolution of wear gaps in fretting problems using the finite element method. The works [19,21] exploited a cycle jump technique to accelerate fretting test simulations, assuming that the contact pressure and the slip distribution remains constant for a given number of cycles. The cycle jumping method has been recently applied also in [22]. Other recent contributions are [23–25]. Finite wear simulations have been explored in [25], where the shape changes are simulated using the Lagrangian multipliers approach.

Wear particle formation and the formation of micro-cracks and crack propagation from the surface have been modeled in [7,26–30] under various operating conditions using fracture mechanics techniques. More recently, debris formation at the asperity level have been simulated using an elasto-plastic FE model in [31,32], at the atomistic level in [33,34], and exploiting the phase-field approach to fracture in [4,35]. A review on the different modeling approaches to wear can be found in [36].

Numerical methods employing BEM or Green's functions-based methods have been proposed to evaluate tangential contact problems

* Corresponding author.
E-mail address: mariarosaria.marulli@imtlucca.it (M.R. Marulli).

https://doi.org/10.1016/j.triboint.2025.111006
Received 23 May 2025; Received in revised form 5 July 2025; Accepted 17 July 2025
Available online 26 July 2025

with complex contact geometries, see [37–40]. In this context, wear simulations using BEM have been conducted in [41–45]. A BEM-based algorithm poses several limitations stemming from the linear elasticity assumptions, half space approximations, and material homogeneity. Consequently, FEM can be used to overcome those limitations, see [46–48] for more details.

Experimental investigations show that, for surfaces under contact, roughness can range from a nano-scale to a milli-scale and plays a crucial role in most engineering applications [49]. Consequently, a proper surface geometry description can significantly improve the wear prediction, as the wear is related to the contact area and to the contact traction distribution. Numerical contact models have been developed to predict contact geometry and the evolution of the rough surfaces due to wear, mostly based on BEM [45,50,51].

Solving rough contact problems using standard finite element models is computationally expensive due to the need for a highly refined mesh for surface discretization and the complexity of contact-search algorithms. Wear further exacerbates these challenges, as it requires remeshing the solid throughout the simulation to account for shape modifications. To the best of the authors' knowledge, FE-based wear simulations have so far been limited to simpler smooth surface geometries, primarily involving conformal contacts, cylindrical or spherical solids, or single asperity models.

To overcome the FE limitations, an efficient variational approach for solving rough contact problems was introduced in [5,52], through the so-called eMbedded Profile for Joint Roughness (MPJR) interface finite elements. This approach proposes a variational formulation to solve rough contact problems considering the interface as nominally flat and embedding an analytic expression or a point-wise defined dataset of roughness to correct the normal gaps inside the interface finite element routine. This allows any shapes of indenters or rough surfaces to be embedded in the contact profile, without the explicit need of a FE discretization of such fine scale details, see [52]. This modeling framework was extended to analyze fully coupled normal and tangential contact problems with complex surfaces in [53] and to ironing problems involving viscoelastic materials in [54]. The method has been tested with both frictionless and frictional contact problems with adhesion [5] and validated against BEM. Furthermore, it has been successfully employed in conjunction with a phase field approach to brittle fracture, to simulate the complex nonlinear coupled problem of contact-induced fracture determined by spherical rough indentation [55], with a very good agreement with experimental data.

In this article, the MPJR numerical framework is further extended to accommodate wear by updating the contact rough surface embedded in the interface finite elements according to a local – microscopically postulated – Archard law. The analysis is here conducted under the hypothesis of small displacements.

Section 2 presents the theoretical and computational aspects related to the numerical computation of wear, followed by a mathematical formulation that includes the prediction of the wear profile. Section 3 presents the variational methods to wear, where the governing equation in the strong and weak forms are derived. The finite element implementation of the wear problem is detailed in Section 4. Section 5 presents benchmark examples and comparisons with experimental and analytical studies. Specifically, three geometries of indenting profiles have been analyzed: flat, cylindrical, and Weierstrass–Mandelbrot (WM) profiles have been simulated under different loading conditions with a detailed analysis for each case. Moreover, the section presents also a discussion on the emergent macroscopically wear coefficient effect. Finally, conclusions are outlined in Section 6.

2. Mathematical formulation

2.1. Wear depth predictions

The variational methods for wear require the definition of bodies under consideration, the computation of the contact domain, strain and stress fields, and frictional effects. This article presents the two-dimensional formulation of a contact problem involving two solids using energy considerations. The presented methodology is directly applicable in 3D by introducing the 3D elevation function of indenting surface and considering the two possible directions for sliding, but this task is left for further investigation.

When two materials are subject to frictional contact, the amount of material removed from the surface is referred to as wear depth. Wear depth can be numerically estimated using the wear profile, which changes as the materials get removed. Measurement of the wear profiles can be seen in [56–58], in rails and rail wheels. See also the analyses in [59–61] on fretting wear.

To formalize, wear is formulated in the related literature with respect to the change in the following quantities [11]:

1. Mass of material removed from solid.
2. Reduction of volume in the material.
3. Reduction in the dimension of the body; Kennedy and Ling [62] suggested a dependency between the wear rate and the normal pressure, sliding velocity, and temperature. In the case of abrasion, the wear rate was found to be proportional to the frictional force.

In order to make the formulation consistent with the numerics, only a two-dimensional formulation is presented. Let A and B be two bodies under frictional contact whose domain is $\Omega_A \in \mathbb{R}^2$ and $\Omega_B \in \mathbb{R}^2$. Define a vector-valued displacement of the body $\mathbf{u}(\mathbf{X},t) : \Omega \times [0,t] \longrightarrow \mathbb{R}^2$, for a position vector $\mathbf{X} \in \Omega$ and t being a pseudo-time in quasi-static simulations. Consequently, for a position vector $(\mathbf{X} \in \Omega_A, \mathbf{X} \in \Omega_B)$, deformation vectors are defined as $(\mathbf{u}_A, \mathbf{u}_B)$. Let $\partial\Omega_A$, and $\partial\Omega_B$ be delimiting boundaries of Ω_A, and Ω_B respectively, then the velocities $(\mathbf{v}_c^+, \mathbf{v}_c^-)$ describe the wearing out boundaries on $(\partial\Omega_A, \partial\Omega_B) \in \mathbb{R}^1$, respectively, mainly due to:

1. Deformation of the bodies $(\mathbf{v}_A, \mathbf{v}_B)$.
2. Wear process $(\mathbf{v}^+, \mathbf{v}^-)$.

where $(\mathbf{v}_A, \mathbf{v}_B)$ are material velocities. Let ρ_A and ρ_B be mass densities, and m_A and m_B describe the rate of mass flowing out of boundaries $\partial\Omega_A$ and $\partial\Omega_B$ due to wear. Then the relationship between the mass $(\mathrm{m}_A, \mathrm{m}_B)$ and the velocities $(\mathbf{v}_A, \mathbf{v}_B)$ can be written as:

$$\begin{aligned} \mathrm{m_A} &= \rho_A \left(\mathbf{v_A} - \mathbf{v_c}^+\right) \cdot \mathbf{n}^+ = -\rho_A \mathbf{v}^+ \cdot \mathbf{n}^+, \\ \mathrm{m_B} &= \rho_B \left(\mathbf{v_B} - \mathbf{v_c}^-\right) \cdot \mathbf{n}^- = -\rho_B \mathbf{v}^- \cdot \mathbf{n}^-, \end{aligned} \tag{1}$$

where $\mathbf{n}^+$ and $\mathbf{n}^-$ are unit normal vectors to the boundaries $\partial\Omega_A$ and $\partial\Omega_B$, respectively. Notice that the term $\left(\mathbf{v_A} - \mathbf{v_c}^+\right)$ is the difference between the material velocities and wearing out of boundary leading to the velocity of the material left subjected to wear. Consequently, wear at the boundaries can be defined as $\mathbf{v}^+ \cdot \mathbf{n}^+ = \mathrm{v}^+$ for $\partial\Omega_A$, and $\mathbf{v}^- \cdot \mathbf{n}^- = \mathrm{v}^-$ $\partial\Omega_B$.

The article [11] assumed that normal pressure and sliding velocities constitute the velocity of wearing out of the solids under contact. Consequently, Rabinowicz [63] defined this process within the context of Greenwood theory such that $\mathbf{v}^+$ defines the velocity at which $\partial\Omega_A$ travels into $\partial\Omega_A$ due to wear. see Fig. 1(a) for a kinematic description of wear. Within the context of the Eulerian description of displacement functions $(\mathbf{u}_A, \mathbf{u}_B)$, the velocities of the displacement (deformation) $(\mathbf{v}_A, \mathbf{v}_B)$ are related as:

$$\mathbf{v}_A = \frac{d\mathbf{u}_A}{dt} = \dot{\mathbf{u}}_A \qquad \mathbf{v}_B = \frac{d\mathbf{u}_B}{dt} = \dot{\mathbf{u}}_B. \tag{2}$$

Consequently, the relative sliding velocities of two bodies $\mathbf{V_{AB}}$ can be written in terms of the displacements rate as

$$\mathbf{V_{AB}} = \left(1 - \mathbf{n}^+ \otimes \mathbf{n}^+\right)\left(\dot{\mathbf{u}}_A - \dot{\mathbf{u}}_B\right), \tag{3}$$

$$= \left(1 - \mathbf{n}^+ \otimes \mathbf{n}^+\right)\left(\mathbf{v_A} - \mathbf{v_B}\right), \tag{4}$$

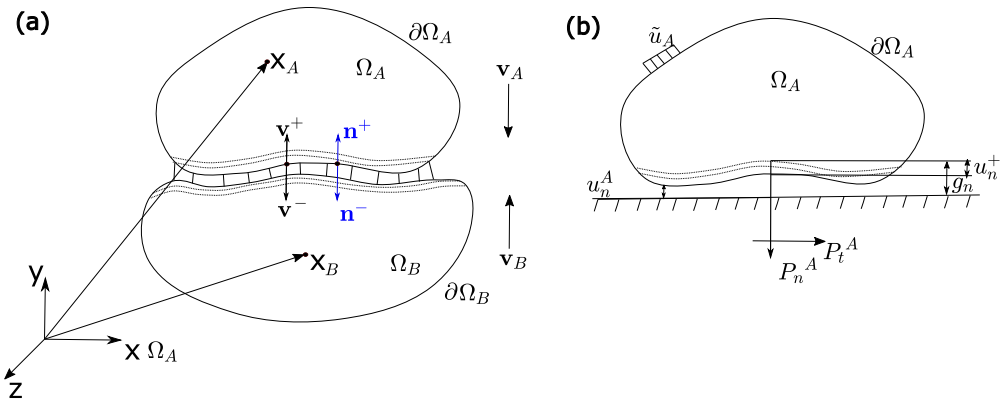

Fig. 1. (a) Kinematics of wear profile wearing out at the boundaries of the solid, (b) simplified geometry for presenting the wear depth (u_n^+), normal and tangential forces (P_n^A, P_t^A), normal gap component between the contact bodies g_n.

where $\otimes$ represents the dyadic product.

The total normal gap (g_n) between two bodies as shown in Fig. 1(b) is defined as a combination of wear depth, and difference in the elastic deformation as

$$\mathrm{g}_n = \left(\mathrm{u}_n^A - \mathrm{u}_n^B\right) + \left(\mathrm{u}_n^+ - \mathrm{u}_n^-\right); \quad \text{on} \quad \partial\Omega_A \cup \partial\Omega_B, \tag{5}$$

where $\left(\mathrm{u}_n^A - \mathrm{u}_n^B\right)$ is the difference in the elastic deformations of two bodies and $\left(\mathrm{u}_n^+ - \mathrm{u}_n^-\right)$ is the wear depth, referred, in the following, with the notation $\Delta u_n = \left(\mathrm{u}_n^A - \mathrm{u}_n^B\right)$ and $w = \left(\mathrm{u}_n^+ - \mathrm{u}_n^-\right)$, respectively.

The elastic deformations of each body at the boundary can be written as:

$$\begin{aligned} \mathrm{u}_n^A &= \left(\mathbf{n}^+ \otimes \mathbf{n}^+\right) \mathbf{u}_A \quad \forall\, \mathbf{x}_A \in \partial\Omega_A, \\ \mathrm{u}_n^B &= \left(\mathbf{n}^- \otimes \mathbf{n}^-\right) \mathbf{u_B} \quad \forall\, \mathbf{x}_B \in \partial\Omega_B. \end{aligned} \tag{6}$$

The total depth of the material removed $\left(\mathrm{u}_n^+\right), \left(\mathrm{u}_n^-\right)$ over a period of time $[0, t]$ can be defined using the velocities as

$$\begin{aligned} \mathrm{u}_n^+ &= \int_0^t \mathrm{v}^+(\mathbf{x}, \tau)\, \mathrm{d}\tau, \quad \forall\ \mathbf{x} \in \partial\Omega_A, \\ \mathrm{u}_n^- &= \int_0^t \mathrm{v}^-(\mathbf{x}, \tau)\, \mathrm{d}\tau, \quad \forall\ \mathbf{x} \in \partial\Omega_B. \end{aligned} \tag{7}$$

where Fig. 1(b) shows the quantities that define the wear depth.

Contact problems and wear predictions require accurate evaluation of stress and strain fields within the solids. Moreover, velocity and tractions at the contact region must be calculated. Naturally, physical conditions have to be met, such as (a) non-penetrating conditions, (b) adhesiveless conditions; these conditions translates to the normal gap to be always greater (when not in contact) or equal to zero (during contact):

$$\mathrm{g_n} \geq 0, \quad \forall\, \mathbf{x} \in \partial\Omega_A. \tag{8}$$

Moreover, the normal contact stress component is less than zero (during contact) or equal to zero (not in contact):

$$\mathrm{P_n^A} \leq 0, \quad \forall\, \mathbf{x} \in \partial\Omega_A. \tag{9}$$

Then, the contact traction $\mathbf{P}_A$ for the solid A, having normal component $\mathrm{P_n^A}$, and tangential component $\mathrm{P_t^A}$ can be written as:

$$\mathbf{P}_n^A = \boldsymbol{\sigma}_A \mathbf{n}^+, \quad \text{on } \partial\Omega_A \tag{10}$$

where $\boldsymbol{\sigma}_A = \mathbb{C} : \boldsymbol{\varepsilon}_A$ is the Cauchy stress tensor. Here $\mathbb{C}$ is the stiffness (elasticity) tensor that relates stress and strain measures. Here $\boldsymbol{\epsilon}$ is the symmetric strain defined as

$$\boldsymbol{\epsilon}(\mathbf{u}) = \frac{1}{2}\left(\nabla\mathbf{u} + \nabla^T\mathbf{u}\right). \tag{11}$$

In the presence of friction with a friction coefficient μ, the tangential traction satisfies

$$|\mathrm{P}_t^A| \leq \mu_A |\mathrm{P}_n^A|. \tag{12}$$

Solving the differential problem subject to the above relationships and to the Dirichlet and Neumann boundary conditions, one can compute the tangential and normal tractions via displacements and displacement gaps. These tangential and normal tractions can be used to calculate, in turn, the wear rate via the local wear law.

Archard [2] formulated that the volume of material removal (W) is directly proportional to the normal contact traction (P_n), the dimensionless wear coefficient (K), the sliding distance (S), and inversely proportional to the hardness (H), i.e.,

$$W = \mathrm{K}\frac{\mathrm{P_n S}}{\mathrm{H}}. \tag{13}$$

The dimensionless wear coefficient K in Eq. (13) can be defined in different ways. From the thermodynamics point of view, the energy (E) necessary for the formation of wear debris (material removed due to wear) having mass m, the following inequalities have to be satisfied for bodies A and B:

$$\mathrm{m}_A \mathrm{E}_A \geq 0, \quad \mathrm{m}_B \mathrm{E}_B \geq 0, \tag{14}$$

meaning that the internal energy consumed during the wear process is non-negative.

Eq. (13) can be formulated also in terms of wear depth w, using the normal contact traction P_N as:

$$w = k_w \mathrm{P_n S}. \tag{15}$$

where k_w is the dimensional wear coefficient assumed to be a material property.

Notice that Archard's wear law does not account for the formation of a third body, which would modify the contact conditions. The current formulation is restricted to the simulation of a two-body wear problem, while the solution of a third body contact has not yet been attempted. A possible way to cope with a third-body contact could be to couple the present method with the methodology in [64], where the third body is incrementally modified in time both in terms of volume (as a function of the predicted debris formation based on the present approach), and in terms of interface mechanical properties associated to the wear debris. On the other hand, the proposed methodology could be applied macroscopically to adhesive wear, often described by a similar macroscopic wear evolution law as the Archard law. For simulation of adhesive wear at the microscale, this can be achieved with little modification by introducing an adhesive potential as already done by the authors in [52], along with plasticity constitutive models for the

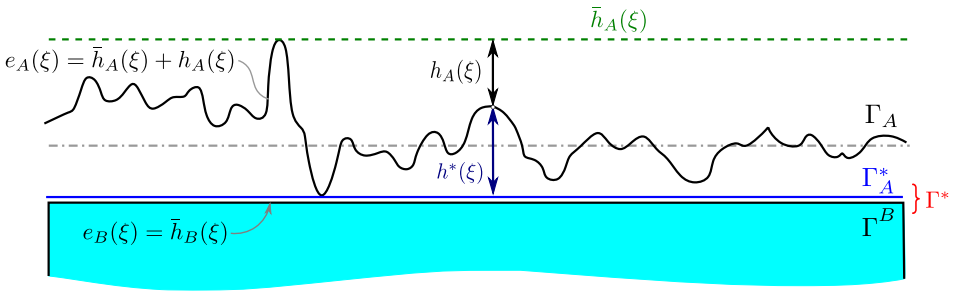

Fig. 2. Embedding of the rough topography of the indenter in the nominally flat interface.

bulk. Other forms of wear, for instance induced by corrosion, are not accounted in the current formulation. This can be a further research direction by setting the present mechanical problem within a multi-field framework to simulate the thermo-chemico-mechanical fields and their coupling. In this regards, the advantage of the proposed variational framework is that it would enable to make energy-based additions in the Clausius–Duhem inequality, changing the energy density function in Eq. (21) and consequently accounting for the energies in Eq. (24).

Furthermore, Archard's wear law assumes a constant wear coefficient, consequently neglecting the material properties apart from hardness: friction, speed of the sliding, effect of lubrication, to name a few.

3. Variational methods to wear

In this section, the initial boundary value problem is developed based on the thermodynamic and energy considerations of the contact problem with embedded roughness as in [52,53] adding the wear contribution.

3.1. Governing equation and strong form

The two solids Ω_A and Ω_B defined in Section 2 are considered to be potentially in contact at the opposite boundaries $\Gamma_i \subset \partial\Omega_i$ $(i = A, B)$ such that the contact interface $\Gamma \in \mathbb{R}^1$ can be defined as $\Gamma = \cup_{i=A,B}\Gamma_i$. The real contact region in the interface Γ_i is represented by Γ^c with $\Gamma^c = \Gamma_A^c \cup \Gamma_B^c$, where Γ_i^c $(i = A, B)$ is the region in body (A, B) in contact. The region Γ_i^c is not normally known a-priori. The distinction between Γ_i^c and Γ_i is introduced because, in case of a nonconformal contact problem, the actual contact region is a subset of the total area that could be potentially in contact, i.e. $\Gamma_i^c \subseteq \Gamma_i$.

Let assume that the contact boundary Γ_B is smooth, while the indenting contact boundary Γ_A has an arbitrary shape that may be specified either by an analytical function (e.g., a parabolic or harmonic profile) or by a set of discrete data related to a more complex rough topology.

The key idea of the approach developed in the authors' previous works consists in simplifying the original boundary of the indenter Γ_A into a flat profile Γ_A^*, while the actual profile (or surface in 3D) of the boundary is embedded point-wise in its exact form into the interface finite element formulation, as depicted in Fig. 2. The geometrical difference between Γ_A and Γ_A^* is mathematically described by an elevation function $e_A(\xi_A)$ where $\xi_A = \xi(\mathbf{X})$ is a curvilinear coordinate system on the indenting profile.

If we defined $\bar{h}_A(\xi_A)$ as the smoothed representation of the rough boundary, given by a curve parallel to the average profile of the boundary and with datum set in correspondence of its deepest valley, the elevation function that maps the indenter actual topography is:

$$e_A(\xi_A) := \bar{h}_A(\xi_A) + \mathrm{h}_A(\xi_A) \tag{16}$$

For the already smooth boundary Γ_B, the elevation function simply reads:

$$e_B(\xi_B) := \bar{h}_B(\xi_B) \tag{17}$$

This method reduces the contact problem to a nominally flat-to-flat interface Γ^* defined by two initially coincident but distinct flat profiles described by $e_B(\xi)$ plus the associated function $h^*(\xi) = \max_\xi [h_A(\xi)] - h_A(\xi)$. At the beginning of the contact problem, the two profiles are considered to be in contact at only one point with zero contact pressure.

The tangential and normal unit vectors for the two sides are equal and opposite of the nominally flat Γ^* interface defined as:

$$\mathrm{t}_A(\xi_A) = -\mathrm{t}_B(\xi_B) \text{ and } \mathrm{n}_A(\xi_A) = -\mathrm{n}_B(\xi_B). \tag{18}$$

At the interface Γ^*, the displacement gap components are further determined as the projection of the relative displacement $\Delta\mathbf{u} = \mathbf{u}_A - \mathbf{u}_B$ into the normal and tangential directions such that $\Delta\mathbf{u} = (\Delta\mathbf{u}_t, \Delta\mathbf{u}_n)^T$.

Within the context of the energy of the system, the total energy of the system under contact along with the interface Γ^* can be written considering the following contributions:

1. The external energy Ψ_{ext} due to the applied boundary conditions such as displacement $\bar{\mathbf{u}}$ and traction $\bar{\mathbf{t}}$.
2. Strain energy/elastic generated by the body Ψ_e.
3. Contact energy Ψ_{cont}.

Hence, the total energy per unit mass per unit volume takes the form:

$$\Pi = \Psi_{ext} + \Psi_e + \Psi_{cont}. \tag{19}$$

Furthermore, the balance principles driving the wear problem have to satisfy the balance of energy and contact profiles:

$$\rho\dot{\mathrm{e}} = \boldsymbol{\sigma}_{ij}\boldsymbol{\epsilon}_{ij}, \quad \text{in} \quad \Omega, \tag{20a}$$

$$\dot{\Psi} = \mathrm{P}_n\dot{g}_n + \mathrm{P}_t\dot{g}_t - \mathrm{P}_c, \quad \text{on} \quad \Gamma^*, \tag{20b}$$

where ρ is the mass density of the body's bulk, $\dot{\mathrm{e}}$ is the body's specific energy, and Ψ is the internal energy of the contact surface. Here, P_n and P_t are the normal and tangential contact traction respectively. Finally, $\dot{\omega}_t$ presented the wear rate, whereas $\dot{(\cdot)} = \frac{\mathrm{d}(\cdot)}{\mathrm{d}t}$ denotes the time derivative. Furthermore, P_c is the entropy density of the system (such as heat generated due to contact).

The Helmholtz free energy density for the linear isotropic material under isothermal conditions takes the form

$$\boldsymbol{\Psi}_e(\mathbf{u}) = \frac{1}{2}\boldsymbol{\varepsilon} : \mathbb{C} : \boldsymbol{\varepsilon} = \frac{1}{2}\lambda\mathrm{tr}^2(\boldsymbol{\varepsilon}) + \mu\boldsymbol{\varepsilon} : \boldsymbol{\varepsilon}, \tag{21}$$

where $\mathbb{C}$ defines the linear elasticity tensor, $\mathbb{C} = 2\mu\mathbb{I} + \lambda\mathbf{1}\otimes\mathbf{1}$ function of Lame's constant λ and μ. Here, $\mathbb{I}$ and $\mathbf{1}$ are fourth-order and second-order identity tensors, respectively. The state laws such as stress can be easily accessible using Helmholtz free energy function as

$$\boldsymbol{\sigma} := \frac{\partial\boldsymbol{\Psi}}{\partial\boldsymbol{\varepsilon}}. \tag{22}$$

In the contact region, similar to the bulk, a standard Clausius–Duhem inequality for the contact interface satisfies:

$$\dot{\Psi} \lesssim \mathrm{P}_n \dot{g}_n + \mathrm{P}_t \dot{g}_t, \quad \text{on } \Gamma^* \tag{23}$$

where Ψ is the internal energy at the interface.

The contribution of the energy due to contact can be written as an additive decomposition of the energy associated with the normal part and the tangential part as:

$$\Psi_{cont} = \Psi_{c,n} + \Psi_{c,t} = \int_{\Gamma^*} P_n \, g_n^* \, \mathrm{d}\Gamma + \int_{\Gamma^*} P_t \, g_t \, \mathrm{d}\Gamma. \tag{24}$$

Furthermore, the contributions stemming from fatigue, fretting wear, oxidation, corrosion, thermo-mechanical loading etc., can be incorporated in the total energy formulation subjected to the mass and energy balance. The tangential contribution is given by the regularization of the Coulomb friction law as done in [53]:

$$P_t = \mu |P_n| \tanh\left(\frac{\dot{g}_t}{\epsilon_t}\right). \tag{25}$$

While the tangential gap g_t depends only on the relative sliding of the two bodies and it is not affected by wear, the normal gap includes three contributions: the relative normal displacement Δu_n, stemming from the solution of the contact problem; the correction to the separation between the nominally flat contact interface to account for the non-planar profile embedded in the MPJR interface finite element h^*; and the material removal due to wear w, which is initially zero and increase with time. Consequently:

$$g_n^* = \Delta u_n + h^* + w = g_n + h^*. \tag{26}$$

Here g_n^* is the corrected normal gap employed in a standard penalty approach to solve the contact problem. The normal contact pressure takes the form:

$$P_n = \begin{cases} K_n g_n^* & \text{if} \quad g_n^* < 0 \\ 0 & \text{if} \quad g_n^* \geq 0 \end{cases} \tag{27}$$

Here P_n^- is used to refer to $|P_n|$ for $g_n^* < 0$.

Recalling Eq. (15), the wear rate can be computed using the Archard law of wear at the local level, assuming that the wear driving force is proportional to the normal contact pressure P_n^-:

$$\dot{w} = k_w P_n^- |\dot{g}_t|. \tag{28}$$

where $\dot{g}_t$ is the sliding rate computed using a finite difference formula: $\dot{g}_t = \left(g_t^{(t)} - g_t^{(t-1)}\right)/\mathrm{d}t$. Considering a quasi-static problem, for a pseudo-time interval $\mathrm{d}t = 1$, the wear gap is computed as:

$$w = k_w P_n^- |g_t^{(t)} - g_t^{(t-1)}|. \tag{29}$$

Furthermore, the normal traction reads:

$$P_n^- = K_n g_n^* = K_n \left(\Delta u_n + h^* + w\right), \tag{30}$$

and introducing Eq. (29) into Eq. (30):

$$P_n^- = K_n \left(\Delta u_n + h^*\right) + K_n k_w P_n^- \, |g_t^{(t)} - g_t^{(t-1)}|. \tag{31}$$

which finally gives an explicit equation for P_n^-:

$$P_n^- = \frac{K_n(\Delta u_n + h^*)}{1 + K_n k_w |g_t^{(t)} - g_t^{(t-1)}|}. \tag{32}$$

From Eqs. (25) and (32), the residual and the stiffness matrix of the interface finite element can be computed for an implicit formulation. Notice that the wear coefficient is set to constant in the proposed model. Consequently, the effect of transverse shear stress is not taken into account. Another possibility is to exploit an explicit approach where the wear contribution is computed considering the normal contact traction at the previous pseudo-time step (explicit formulation):

$$w^{t-1} = k_w \left(P_n^-\right)^{t-1} |g_t^{t-1} - g_t^{t-2}|. \tag{33}$$

Consequently, the normal contact pressure would read:

$$P_n^- = K_n \left(\Delta u_n + h^* + w^{t-1}\right) = K_n \left(\Delta u_n + h^*\right) + K_n k_w \left(P_n^-\right)^{t-1} \, |g_t^{t-1} - g_t^{t-2}|. \tag{34}$$

In this article, we adopt Eq. (33) to compute the wear gap and the Eq. (34) to compute the normal contact pressure. As a consequence of the explicit treatment of wear evolution, the derivative of the normal pressure becomes independent of the wear profile, with an easier finite element solution of the coupling of the wear rate with the contact energy function.

Now, substituting Eq. (21), (24) into Eq. (19), leads to the following pseudo internal energy

$$\Pi = \int_\Omega \frac{1}{2} \boldsymbol{\epsilon} : \mathbb{C} : \boldsymbol{\epsilon} \mathrm{dV} + \int_{\Gamma^*} P_n \, g_n^* \, \mathrm{d}\Gamma + \int_{\Gamma^*} P_t \, g_t \, \mathrm{d}\Gamma + \Psi_{ext}. \tag{35}$$

Now, Eq. (35) is solved for the displacement $\mathbf{u}$ and the relative displacement $\Delta\mathbf{u}$. Later, the actual gaps are estimated using the correction related to the composite topography. Subsequently, wear rate and contact pressures are computed from the primary displacement variables as detailed above. The external work $\Psi_{ext}(\mathbf{u})$ due to the applied loading can be defined as

$$\Psi_{ext}(\mathbf{u}) := \int_\Omega \boldsymbol{f_v} \cdot \mathbf{u} \, \mathrm{d}V + \int_{\partial\Omega} \bar{\mathbf{t}} \cdot \mathbf{u} \, \mathrm{dS}. \tag{36}$$

Here, $\bar{\mathbf{t}} = \boldsymbol{\sigma} \cdot \mathbf{n}$ on $\partial\Omega^N$ is the traction with an outwards unit normal $\mathbf{n}$ (Neumann boundary condition) and $\boldsymbol{f_v} : \Omega \to \mathbb{R}^2$ is the body force.

Naturally, the solution $\mathbf{u}$ for the total energy functional Π at the interface in Eq. (35) in the quasi-static setting can be derived by considering the first variation of the functional, i.e.,

$$\delta\Pi(\mathbf{u}) = \frac{\mathrm{d}}{\mathrm{d}e} \Pi(\mathbf{u} + e\delta\mathbf{u}) \Big|_{e=0} = 0, \tag{37}$$

For a given initial boundary condition, the problem reduces to finding $\mathbf{u}$ such that, for each $\mathrm{t} \in [0, \mathrm{T}]$:

$$\begin{aligned} \int_\Omega \boldsymbol{\epsilon}(\mathbf{u}) : \mathbb{C} : \boldsymbol{\epsilon}(\delta\mathbf{u}) \, \mathrm{dV} + \int_{\Gamma^*} \mathrm{P}_n(\Delta\mathbf{u}) \mathrm{g}_n^*(\Delta\delta\mathbf{u}) \, \mathrm{d}\Gamma \\ + \int_{\Gamma^*} \mathrm{P}_t(\Delta\mathbf{u}) \mathrm{g}_t(\Delta\delta\mathbf{u}) \, \mathrm{d}\Gamma + \Psi_{ext}(\mathbf{u}) = 0 \end{aligned} \tag{38}$$

for $\delta\mathbf{u} \in \mathcal{V} := \{\delta\mathbf{u} \in \mathrm{H}(\Omega) \times [0, T]; \delta\mathbf{u} = 0 \ \text{ on } \ \partial\Omega_{\mathbf{u}}\}$.

4. Finite element implementation

The numerical treatment to solve the weak form in Eq. (38) involves the introduction of a finite element discretization for the bulk Ω and the interface Γ^*. Notice that the bulk Ω is subdivided into Ω_A and Ω_A.

We define the discretization of the bulk $\Omega \to \Omega_i^h$ and the interface $\Gamma^* \to \Gamma^{*h}$ for some discrete mesh $\mathbf{h}$ such that partition of unity and the compactness of the isoparametric function in Ω_i^h and Γ^{*h} is preserved. The displacement field $\mathbf{u}$ and the strain $\boldsymbol{\epsilon}$ are interpolated in terms of the nodal displacement $\mathbf{d}$ as follows,

$$\mathbf{u}(\mathbf{x}) = \mathbf{N}(\mathbf{x})\mathbf{d} \qquad \boldsymbol{\epsilon} = \mathbf{B}(\mathbf{x})\mathbf{d}, \tag{39}$$

where $\mathbf{N}(\mathbf{x})$ is the matrix that contains the shape function, and $\mathbf{B}(\mathbf{x})$ defines its corresponding spatial derivative. Similarly, the test function $\delta\mathbf{u}$ and the corresponding strain $\boldsymbol{\epsilon}(\delta\mathbf{u})$ takes the form

$$\delta\mathbf{u}(\mathbf{x}) = \mathbf{N}(\mathbf{x})\delta\mathbf{d}; \qquad \boldsymbol{\epsilon}(\delta\mathbf{u}) = \mathbf{B}(\mathbf{x})\delta\mathbf{d}, \tag{40}$$

This interpolation scheme applied to the weak form leads to the following discrete residual vector:

$$\mathrm{R}^u = \int_\Omega \mathbf{B}^T : \boldsymbol{\sigma} \, \mathrm{dV} - \int_\Omega \mathbf{N}^T \cdot \mathbf{f}_\mathrm{v} \, \mathrm{dV} - \int_{\partial\Omega} \mathbf{B}^T \cdot \bar{\mathbf{t}} \, \mathrm{dS}. \tag{41}$$

Moreover, the tangent stiffness matrix of the bulk reads

$$\mathbf{K}_{uu} = \frac{\partial \mathbf{R}^u}{\partial \mathbf{d}} = \int_\Omega \mathbf{B}^T \mathbb{C} \mathbf{B} \, \mathrm{dV}. \tag{42}$$

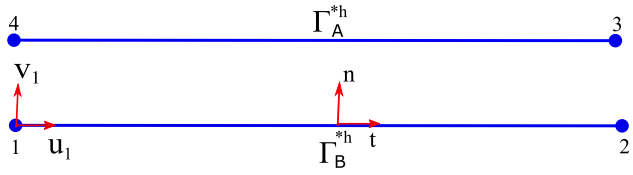

Fig. 3. Interface finite element topology.

The finite element approximation of bulk takes the form

$$\mathbf{K}_{uu}\,\mathbf{d} = \mathbf{R}^{u}, \tag{43}$$

where the above equation is solved for $\mathbf{d}$ through a system of linear equations, if the material constitutive relation is linear.

At the interface Γ^{*h}, a conforming finite element discretization is assumed. The interpolation of the interface is carried out by the displacement field $\mathbf{u}$ of the bulk in the discrete domain Ω. Consequently, the interface finite element with embedded roughness is introduced, capable of handling wear and friction (see Fig. 3).

Let $\mathbf{d}$ be the collection of generalized displacements for the four-node interface as:

$$\mathbf{d} = \{u_1, v_1, u_2, v_2, u_3, v_3, u_4, v_4\}^T. \tag{44}$$

The contribution of the interface to the weak form is:

$$\int_{\Gamma^*} \mathrm{P}_n(\Delta\mathbf{u})\, \mathrm{g}_n^*(\Delta\delta\mathbf{u})\, \mathrm{d}\Gamma + \int_{\Gamma^*} \mathrm{P}_t(\Delta\mathbf{u})\, \mathrm{g}_t(\Delta\delta\mathbf{u})\, \mathrm{d}\Gamma, \tag{45}$$

whose interpolated finite element form is:

$$\int_{\Gamma^*} \mathrm{P}_n(\Delta\mathbf{u})\, \mathrm{g}_n^*(\Delta\delta\mathbf{u})\, \mathrm{d}\Gamma \approx \mathrm{A}_{e=1}^{nel} \lim \left\{ \int_{\Gamma_e^*} \mathrm{P}_n(\Delta\mathbf{u})\, \mathrm{g}_n^*(\Delta\delta\mathbf{u})\, \mathrm{dS} \right\}, \tag{46}$$

and

$$\int_{\Gamma^*} \mathrm{P}_t(\Delta\mathbf{u})\, \mathrm{g}_t(\Delta\delta\mathbf{u})\, \mathrm{d}\Gamma \approx \mathrm{A}_{e=1}^{nel} \lim \left\{ \int_{\Gamma_e^*} \mathrm{P}_t(\Delta\mathbf{u})\, \mathrm{g}_t(\Delta\delta\mathbf{u})\, \mathrm{dS} \right\}. \tag{47}$$

Here the subscript 'e' refers to the eth interface element such that $\mathrm{e} \in \{1, \ldots ....., \mathrm{nel}\}$ and 'A' refers to a symbolic assembly operator. The integral in the above equation can be computed using the two-point Newton–Cotes quadrature formula. The details of the FE formulation is omitted for the sake of brevity, while the readers are referred to [5,52,53] for more details.

The discrete residual is then computed as:

$$\mathbf{R}_{\mathrm{e}}^{(k)} = \int_{\Gamma^*} \mathbf{L}^T\mathbf{N}^T\mathbf{R}^T\mathbf{P}\ \mathrm{d}\,\Gamma, \tag{48}$$

with $\mathbf{P} = (\mathrm{P_t}, \mathrm{P_n})$ collecting the tangential and normal contact pressures computed from Eq. (25) and (34), respectively. Furthermore, the stiffness matrix for the interface reads

$$\mathrm{K}_{\mathrm{e}}^{(k)} = \int_{\Gamma^*} \mathbf{L}^T\mathbf{N}^T\mathbf{R}^T\mathbb{C}_c\mathbf{R}\mathbf{N}\mathbf{L}\ \mathrm{d}\Gamma, \tag{49}$$

where the linearized interface constitutive matrix $\mathbb{C}_c$ takes the form:

$$\mathbb{C}_c = \begin{bmatrix} \dfrac{\partial \mathrm{P_t}}{\partial \mathrm{g_t}} & \dfrac{\partial \mathrm{P_t}}{\partial \mathrm{g_n}} \\ \dfrac{\partial \mathrm{P_n}}{\partial \mathrm{g_t}} & \dfrac{\partial \mathrm{P_n}}{\partial \mathrm{g_n}} \end{bmatrix}. \tag{50}$$

The expressions for each components of $\mathbb{C}_c$ for $g_n^* < 0$ are:

$$\frac{\partial \mathrm{P_t}}{\partial \mathrm{g_t}} = \frac{\mu|\mathrm{P}_n|}{\epsilon_T}\left[1 - \tanh^2\left(\frac{\dot{g}_t}{\epsilon_T}\right)\right], \tag{51a}$$

$$\frac{\partial \mathrm{P_t}}{\partial \mathrm{g_n}} = \frac{\mu K_n g_n^*}{|g_n^*|}\tanh\left(\frac{\dot{g}_t}{\epsilon_T}\right), \tag{51b}$$

$$\frac{\partial \mathrm{P_n}}{\partial \mathrm{g_t}} = 0, \tag{51c}$$

Table 1
Geometrical and model parameters for the flat indenter simulations.

Model parameter	Value
Interface size	10 mm
Substrate size	20 mm
Substrate thickness	10 mm
Substrate Young Modulus	80 GPa
Poisson ratio	0.22
Friction coefficient	0.2
Local wear coefficient	10^{-7} MPa^{-1}
Penalty parameter	10^6 N/mm^3

$$\frac{\partial \mathrm{P_n}}{\partial \mathrm{g_n}} = K_n. \tag{51d}$$

5. Exploitation of the proposed approach for virtual testing

This section proposes benchmark examples to illustrate the efficiency and applicability of the proposed wear model using three types of indenting profiles: cylindrical, flat, and rough indenters. The specific examples demonstrate the potentiality of the MPJR interface finite element approach and its finite element implementation by a detailed analysis of the resulting normal and tangential contact tractions, wear profiles and wear rates.

The embedded roughness methodology allows to model all the cases as a nominally flat indenter acting on a linear elastic rectangular substrate. The indenter profile elevation is then analytically embedded in the MPJR interface finite elements for each case, and computed at every Newton–Cotes integration point of the discretized problem. The simulations are analyzed in plane strain conditions.

5.1. Flat indenter

This section is dedicated to the case of a flat punch indenting a linear elastic isotropic substrate with linear and cyclic loading. The geometry of the test, the employed finite element mesh, and the boundary conditions are shown in Fig. 4. Notice that the global reference system is set such that the interface coordinates vary in the interval $-5\ \mathrm{mm} \le x \le 5\ \mathrm{mm}$. The model parameters are summarized in Table 1. At first, the simulations regarding the linear loading will be discussed, followed by a discussion on the cyclic loading.

5.1.1. Linear loading

This section aims at studying the effects of wear in the linear loading case. For this simulation, the bottom edge of the substrate is fully constrained, while the normal and tangential displacement of $\bar{u}_y$ and $\bar{u}_x$ are imposed on the top edge of the punch, respectively, with a temporal sequence shown in Fig. 5. Specifically, a monotonically increasing normal displacement (vertically downwards) up to 0.5 mm is applied until $t_s = 20$, and then held constant. Meanwhile, a tangential displacement (horizontal towards right) is applied at time $t_s = 20$, monotonically increasing till the value of $\bar{u}_x = 2$ mm is reached at the end of the simulations. This loading sequence ensures the contact between the two bodies before applying any tangential load. In order to simplify the notations, the phase where only normal displacement is applied is referred to as *normal loading phase*, while the phase where the normal displacement is held and the tangential displacement is monotonically increased ($20 < t_s < 120$) is referred to as *tangential loading phase*. Notice that the defined boundary conditions lead to elastic deformation of the substrate due to the interaction with the indenter. The choice of such boundary conditions was to prove the potentiality of the approach to handle situations where elastic coupling affects the slip state interactions. However, the displacement of the substrate is very small compared to the size of the specimen. Consequently, the majority

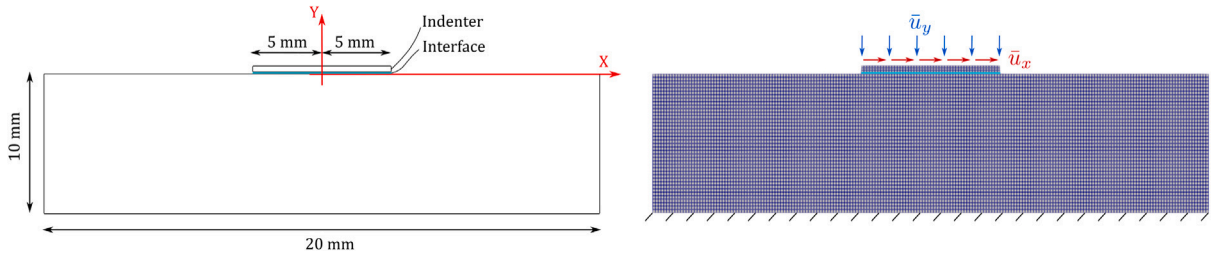

Fig. 4. Flat indenter geometry, mesh discretization, and applied boundary conditions.

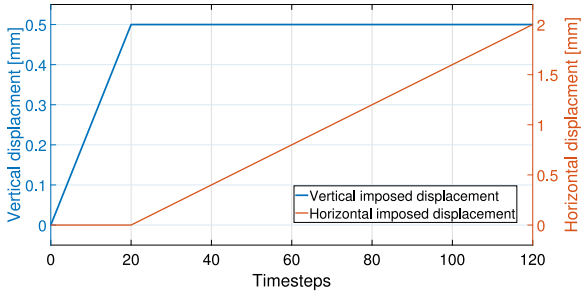

Fig. 5. Normal and tangential displacements imposed at the indenter during the simulation.

of the deformations accumulate near the interface, affecting the contact slip state.

The normal gap correction due to the indenter profile to be used in Eq. (34) in this case is $h^* = 0$, because of the punch profile is flat. Consequently, at the beginning of the simulation, the separation equals the actual gaps computed from the displacement field. The separation, however, evolves during the simulation because of the wear, which causes material loss and modifies the contact geometry.

The contour plots of the normal and tangential displacement of the solids at different time steps are shown in Fig. 6. In the normal loading phase, the displacement is dominated by the $\bar{u}_y = 0.5$, while the displacement in the y-direction is almost zero. During the tangential loading phase, the displacements in the y-direction remain almost constant since a constant $\bar{u}_y = 0.5$ mm is hold, and the only changes are caused by wear that modifies the contact geometry. Furthermore, the displacements in the x-direction in the substrate increase as a result of the frictional interaction with the indenter. At the end of the simulation, the contour plot in Fig. 6(d) shows that the horizontal displacement reaches the maximum and minimum values along the contact surface under the two corners of the indenter. Correspondingly, the horizontal displacement of the two upper edges of the substrate has a value of ≈0.05 mm, which is non-zero because of the elastic coupling, much smaller than the displacement imposed to the rigid indenter (2 mm).

The evolution of the reaction forces during the simulation is shown in Fig. 7. The normal reaction force increases to the value P_m at the pseudo-time step $t_s = 20$, which corresponds to the end of the purely normal loading stage. For a simulation without wear, the value of the normal reaction force would remain constant when the applied normal displacement is kept constant. The wear effect decreases the normal force along with the application of the tangential displacement. The material loss due to wear, in fact, causes, for a constant value of $\bar{u}_y$, the increase of the separation gap between the contact interfaces and the consequent decrease of the contact pressure (which is depicted in detail in the following paragraphs) and of the normal reaction force. The same trend can be recognized for the tangential reaction force, which increases to a maximum value at the time step $t_s = 33$ (corresponding to the full slip condition described in the following) and then decreases.

Fig. 8 presents the normal (in red) and tangential (in black) tractions along the interface when the indenter is pushed against the substrate in the normal direction in (a) and during the tangential loading phase till the full sliding condition (b). The normal traction values, σ_n, have been rendered dimensionless with respect to the flat punch half size a_0 and the maximum value of normal force P_m reached at the time step $t_s = 20$. The tangential tractions have been rendered dimensionless via the coefficient $a_0/(\mu P_m)$. In Fig. 8, it is possible to observe the presence of a symmetric central stick area and two lateral regions of forward and backward slip, corresponding, respectively, to the positive and negative tangential tractions' areas. This initial condition matches with the results obtained with similar simulations conducted in [65] and the references therein, where the wear phenomenon was not included. From this condition, the progressive evolution of contact to full slip (when the tangential traction overlaps everywhere the normal contact traction) is shown in Fig. 8(b). Finally, the evolution of the contact tractions after full slip, during gross sliding, is shown in Fig. 9, where the normal contact tractions decrease because of the effect of wear. The tangential contact traction decreases consequentially, keeping the overlapping with the normal contact tractions.

The evolution of the wear rate is shown in Fig. 10. In the first part of the simulation, the wear rate in the forward and backward slip areas increases with the pseudo-time step, while it remains zero in the central stick area. In the slip zones, non-zero values of the relative tangential displacement between the two contact interfaces occur, and, consequently, there is a non-zero sliding velocity $\dot{g}_t$. Since the proposed wear model computes the material removal according to Eq. (28), and the tangential tractions are computed using a regularization of the Coulomb friction law, as in Eq. (25), which introduces in the model a smooth transition between stick and slip areas, there is a very small wear contribution in the slip areas subjected to a non-zero contact pressure caused by the elastic coupling between the normal and the tangential directions.

A rapid increase in the wear rate can be seen in Fig. 10(a). When the full slip condition is reached, the wear rate differs from zero in the entire domain. In the full sliding phase, both normal and tangential tractions tend to decrease due to the wear. Since no additional load is added, the wear rate starts decreasing due to the decrease in the tractions as shown in Fig. 10(a). This interaction between wear and normal tractions can be seen according to Eq. (34).

It is important to note that the material removal rate shown in Fig. 11 depends on the normal contact pressure and the relative sliding distance according to the Archard law, which has been postulated to apply at the microscopical scale. For this reason, the material removal

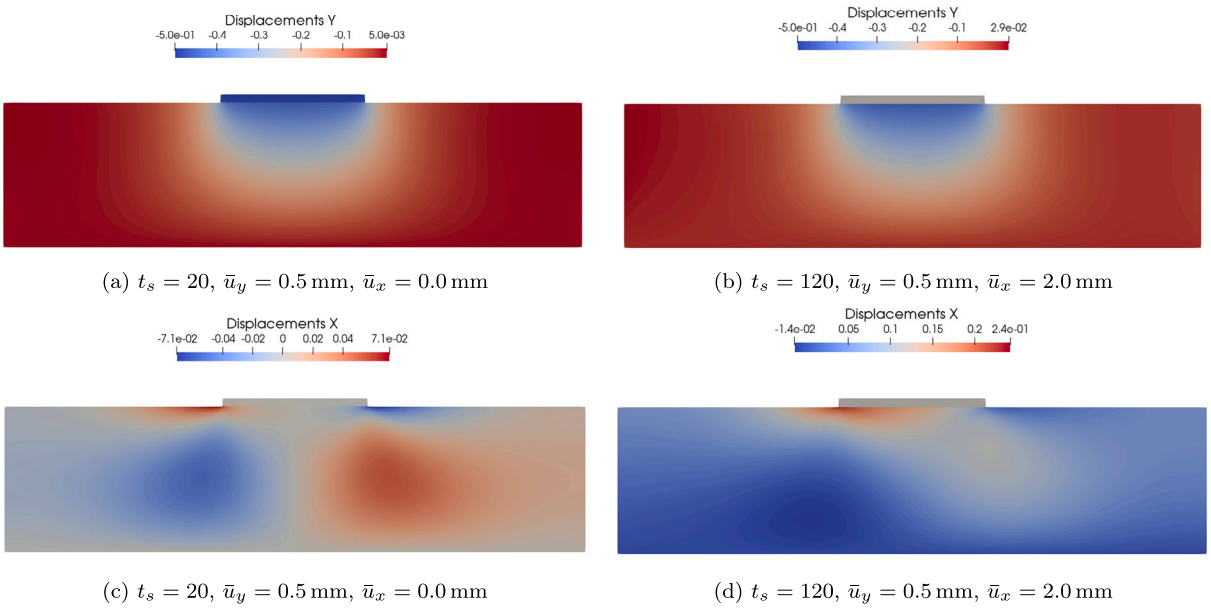

(a) $t_s = 20$, $\bar{u}_y = 0.5\,\text{mm}$, $\bar{u}_x = 0.0\,\text{mm}$

(b) $t_s = 120$, $\bar{u}_y = 0.5\,\text{mm}$, $\bar{u}_x = 2.0\,\text{mm}$

(c) $t_s = 20$, $\bar{u}_y = 0.5\,\text{mm}$, $\bar{u}_x = 0.0\,\text{mm}$

(d) $t_s = 120$, $\bar{u}_y = 0.5\,\text{mm}$, $\bar{u}_x = 2.0\,\text{mm}$

Fig. 6. Contour plots of the normal displacements in (a) and (b), and of the tangential displacements in (c) and (d) at different pseudo-time steps t_s.

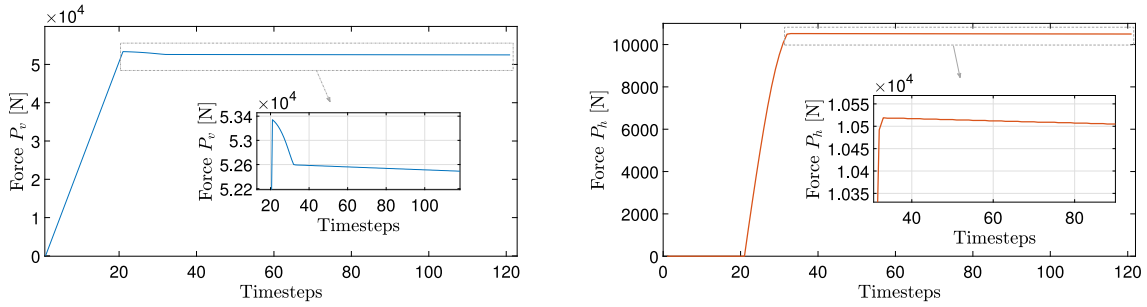

(a) Normal reaction force

(b) Tangential reaction force

Fig. 7. Normal and tangential reaction forces during the simulation.

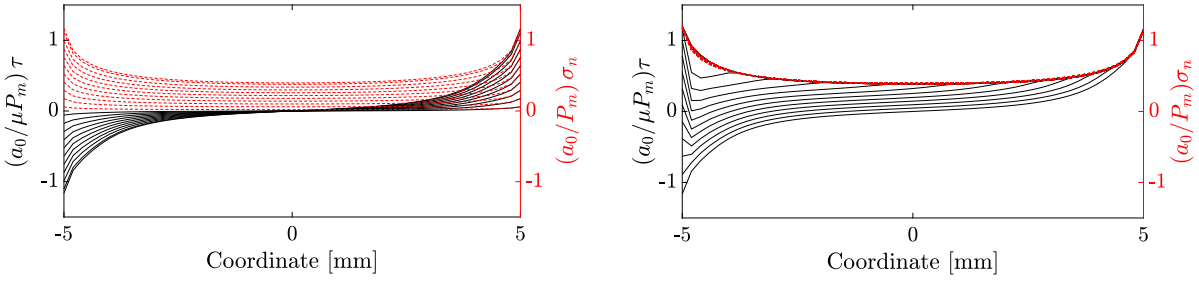

(a) Normal loading phase

(b) Tangential loading phase

Fig. 8. Contact tractions evolution when the normal imposed displacement is linearly increased from zero to its maximum value in (a), and for constant normal displacement and increasing tangential displacement up to full sliding in (b).

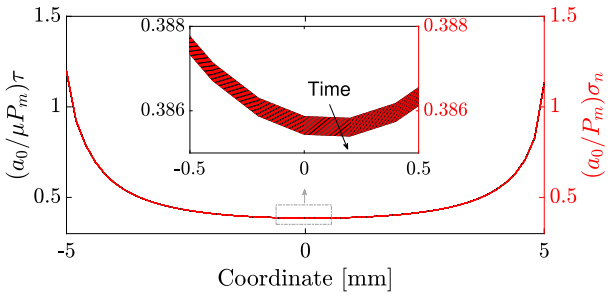

Fig. 9. Normal and tangential contact tractions evolution during full sliding (constant sliding phase).

is higher near the edges of the indenter. Moreover, the material removal is not symmetric, but it reaches higher values on the right side (leading edge) than on the opposite side (trailing edge). The Fig. 12 presents the material removal rate at $t_s = 26$ and at the end of the simulation. The plot shows the asymmetrical material removal due to the imposed horizontal displacement. Initially, the asymmetry between the trailing edge and the leading edge is more visible, while after the tangential loading phase is complete, the difference reduces since the whole contact interface is in slip condition. This asymmetry is amplified even more as the tangential sliding velocity increases, as shown in the following section.

5.1.2. Cyclic loading

The simulation presented in this section shows the potentiality of the proposed approach to deal with wear simulations in case of cyclic loading, which is very common in the experimental tests and applications. The boundary conditions are similar to the linear case: the bottom edge of the substrate is fully constrained, and a monotonically increasing normal displacement $\bar{u}_y$ is applied vertically downwards until $t_s = 20$ and kept constant till the end of the simulation to ensure the contact conditions. Meanwhile, a cyclic tangential displacement (horizontal towards right) is applied from $t_s = 20$ to $t_s = 40$, with the maximum tangential displacement ranging between 2 mm (towards the left) and 2 mm (towards the right) as shown in Fig. 13.

Keeping the same convention as in linear case, the loading can be divided as normal loading phase ($0 < t_s < 20$), and cyclic tangential loading phase ($20 < t_s < 200$). The resulting normal and the absolute value of the tangential reaction forces are presented in Fig. 14(a) and (b) respectively. As a consequence of the wear effects, the normal forces decrease with time as shown in Fig. 14(a). Moreover, the same trend can be observed for the tangential loading. Due to the cyclic loading, the drop in the tangential reactions can be seen as in Fig. 14(b).

Fig. 15 presents the material removal due to the cyclic loading. As the number of tangential loading cycles increases, the material removal increases as in Fig. 15(a) which presents the overall material removal, from which two curves has been selected and depicted in Fig. 15(b) corresponding to $t_s = 20$ and $t_s = 40$, to show the difference in the wear depth at the end of the normal loading phase, and after the first horizontal displacement which corresponds to the situation in Fig. 12, but with different sliding velocities.

5.2. Cylindrical indenter

This section presents the case of an indenter with a cylindrical profile under different loading scenarios. As done for the flat indenter case, the simulation is conducted considering first a simpler linear loading case, and then a more realistic cyclic loading.

Table 2
Geometrical and material parameters used for the cylindrical indenter simulations.

Model parameter	Value
Cylinder radius	$10 \div 120$ mm
Interface size	20 mm
Substrate thickness	5 mm
Cylinder's Young Modulus	210 GPa
Substrate's Young Modulus	80 GPa
Poisson ratio	0.22
Friction coefficient	0.2
Local wear coefficient	10^{-7} MPa^{-1}
Penalty parameter	10^6 N/mm^3

5.2.1. Linear loading

In the first part of the section contains a detailed analysis of the contact problem between a cylindrical indenter having radius $R = 100$ mm and a deformable substrate. In the second part, the results for indenters with different radii ranging from 10 mm to 120 mm are compared. As discussed earlier, the proposed numerical approach avoid the explicit discretization of the indenting profiles using the MPJR interface finite elements. Consequently, the same FE model can be parametrically used to embed many surfaces of different shapes without changing the underlying mesh, assuming that the employed mesh can capture the variation of the indenter shape and the contact areas. In particular, all the cylindrical indenters have been simulated using the geometry and the mesh depicted in Fig. 16, and their profiles have been embedded via the elevation function h^* defined in Eq. (52) as:

$$\mathrm{h}^* = R - \sqrt{R^2 - \chi^2}. \tag{52}$$

Here R is the radius of the indenter, and χ is the coordinate of the integration point.

Compared to the previous case, the actual contact problem is not conformal. For this reason, the indenter block and the interface cover the entire surface of the substrate, such that the evolution of the contact area will always be contained in the interface and there will be no need for contact search algorithms. The boundary conditions and load histories are the same used in the flat indenter case in Section 5.1.1. The model parameters are collected in Table 2.

Fig. 17 presents the contour plot of the displacement field in the $x-$ and $y-$directions for the cylinder radius of $R = 100$ mm. It is immediately possible to notice that the contour plots follow the distributions typical of the contact between a cylinder and a substrate, even though the indenter geometry in the model is simplified as a rectangular block, thanks to the embedded geometry into the MPJR interface finite elements. During the normal loading phase, the penetration of the cylinder into the substrate can be seen in Fig. 17(a) and (c). The transition to the full slip condition can be seen in Fig. 17(b) and (d), which are obtained for the applied displacements $\bar{u}_y = 0.5$ mm, $\bar{u}_x = 2.0$ mm.

The tangential and normal reaction forces during the simulation are shown in Fig. 18. Due to the applied loading condition, the normal reactions reached their maximum value at time step $t_s = 20$, when the system is purely normally loaded. Moreover, tangential reactions remain zeros until the tangential load is applied, when the tangential reaction monotonically increases and reaches its peak at the time step $t_s = 33$ corresponding to the full slip condition. Due to the effect of wear, there is a decrease in both normal and tangential reactions as shown in Fig. 18, in analogy with the flat indenter results.

Moreover, Fig. 19(a) shows the interfacial distribution of normal tractions (in red) and tangential tractions (in black) during the normal loading stage ($t_s = 0 - 20$). Differently from the flat punch, the dimensionless form has been here conducted considering the variation of the contact radius a_0 during the simulation, and the maximum value of the reaction force P_m at the pseudo-time step $t_s = 33$. As expected, the normal force increases to a peak, and the tangential tractions are antisymmetric, creating forward and backward slip areas where wear occurs. As the tangential loading is applied, the dimensionless

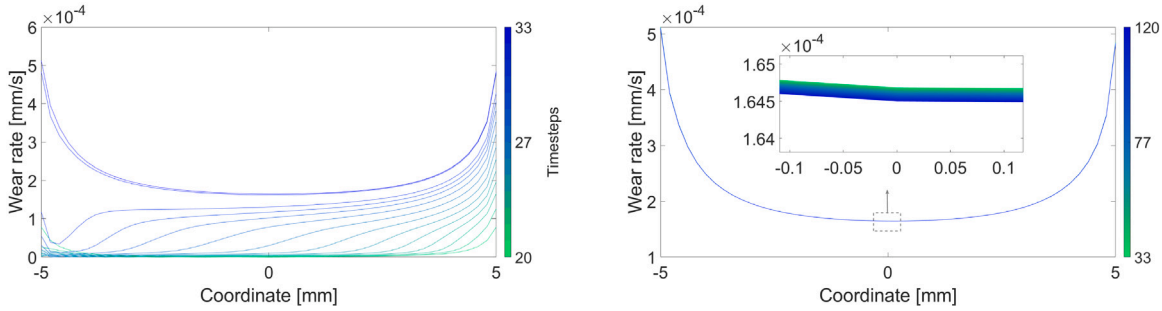

(a) Tangential loading phase till full sliding (b) Tangential loading phase after full sliding

Fig. 10. Wear rate during the flat indenter simulation.

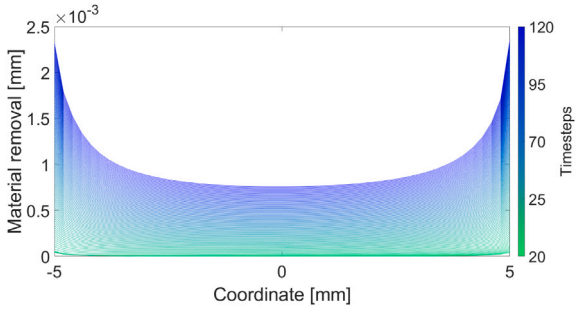

Fig. 11. Material removal due to wear during the tangential loading phase.

tangential force increases, as shown in Fig. 19(b). The progressive evolution of the tangential tractions coincides with the normal tractions when the full slip condition is met, as previously demonstrated in [53].

As a consequence of the contact tractions, the wear rate during the normal loading phase is shown during the tangential loading phase is shown in Fig. 20(a). After the full slip condition is reached, the wear rate naturally slows down, as shown in Fig. 20(b), which corresponds to the pseudo-time steps from $t_s = 34$ to 120.

The predicted material removal during the tangential loading phase is shown in Fig. 21.

In order to study the effect of the indenter radius, simulations corresponding to $R = 10, 20, 50, 80, 100, 120$ mm are compared. The resulting dimensionless contact tractions are depicted in Fig. 22. Specifically, the plots represents the dimensionless normal tractions $\sigma_n/\sigma_{n,max}$, and tangential tractions τ/τ_{max} along the contact interface. It can be noticed that the contact traction distributions follow the same trends found in [5] where the MPJR approach has been validated in absence of wear.

The effect of wear is shown in Fig. 23, which shows the wear rate and the material removal, due to the variation of the indenter radius. It can be noticed that as the radius increases, the contact area increases, leading to more spread normal and tangential tractions. Consequently, the material removal is distributed over a larger area, decreasing the maximum material removal in the center of the indenter.

5.2.2. Cyclic loading

With the goal of validating the proposed computational framework, the case of a rigid cylindrical indenter of radius $R_s = 5$ mm in contact with a steel substrate (young's Modulus $E = 210$ GPa and Poisson ratio $\nu = 0.3$) is described in this section. The FE model resembles the one used in the previous section, however a substrate size of 4 mm×5 mm has been employed to account for the smaller contact area compared to the previous cases. The cylindrical indenter is subject to a constant vertical normal force of 50 N, and to an harmonic tangential displacement having amplitude of 2 mm for a total of 1000 cycles and a total sliding distance of 4m. This setup has been inspired by the experimental test conducted in [12] which have been used also for the validation of the analytical model proposed in [8]. Both the experimental and the analytical results available in the literature regard a spherical pin indenting on a steel plate, however, for simplicity, the simulation presented in this work is two-dimensional, reproducing a cylindrical indenter. The results of the MPJR approach are presented in Fig. 24 which shows that the proposed approach is capable of reproducing the experimental and analytical trends typical of Hertzian contacts.

The same simulation results have been also compared with the asymptotic model predictions in [9] and the experimental results in [19] in terms of peak contact pressure and half width contact variations for cylinder-on-flat tests, see Fig. 25. The literature data are related to the case of a cylindrical indenter radius of radius 12 mm subject to a vertical load $F = 185$ N and to a cyclic tangential displacement having amplitude 0.05 mm. Even in this case, the proposed approach reproduces very well the trend available in the literature.

5.3. Rough indenter

A fractal profile as a model for roughness is examined in this section to test the potentiality of the proposed numerical framework for complex embedded geometries and fine scale resolutions for which the finite element method, to the best of the authors' knowledge, has never been attempted before.

In particular, the Weierstrass–Mandelbrot (WM) function is used to create the complex contact surfaces of several rescaled harmonic components. Even though many other functions can be utilized in the proposed framework to generate and assimilate the elevation produced by the complex surface, the WM function offers unique challenges regarding the numerical implementation and demands high-precision computation. Hence, the WM function is chosen to showcase the robustness and versatility of the presented computational framework in a high-fidelity framework.

The elevation field given by the rough profile can be generated as a fractal function with harmonic given by:

$$h^* = g_0 \sum_{n_w=0}^{\infty} \gamma^{(D-2)n_w} \cos\left(2\pi \frac{\gamma^{n_w} \chi}{\lambda_0}\right), \tag{53}$$

where χ is the integration point x-coordinate along the interface, g_0 is the amplitude of the biggest cosine function, n_w is the number of harmonics. Furthermore, λ_0 is the largest scale roughness' wavelength, γ is a parameter related to the waves amplitude, and D is the fractal dimension taking values $1 \leq D \leq 2$ [66]. The cosine function is summed over n_w to create a superposition of the sinusoidal waves of wavelength $\lambda_{n_w} = \dfrac{\lambda_0}{\gamma^{n_w}}$, and amplitude $g_{n_w} = g_0 \gamma^{(D-2)n_w}$, with $\gamma > 1$.

The two rough profiles chosen for the numerical simulations presented in this section are shown in Fig. 26 and the employed parameters for their generation through the Eq. (53) are collected in Table 3. As a balance between computational efficiency and the complexity of the

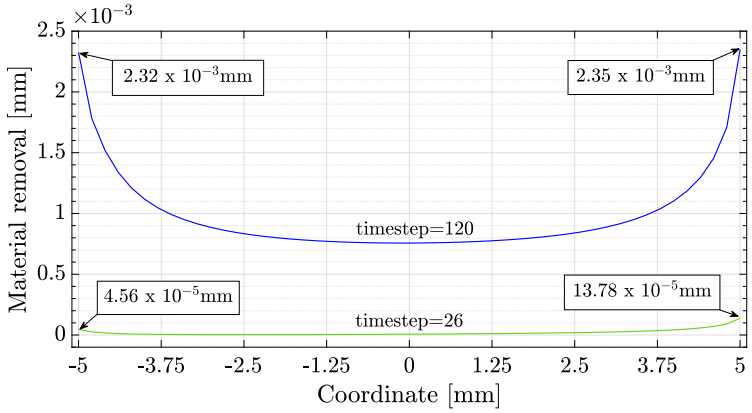

Fig. 12. Material removal at two different timesteps of the flat indenter simulation, showing higher material removal at the leading edge than at the trailing edge.

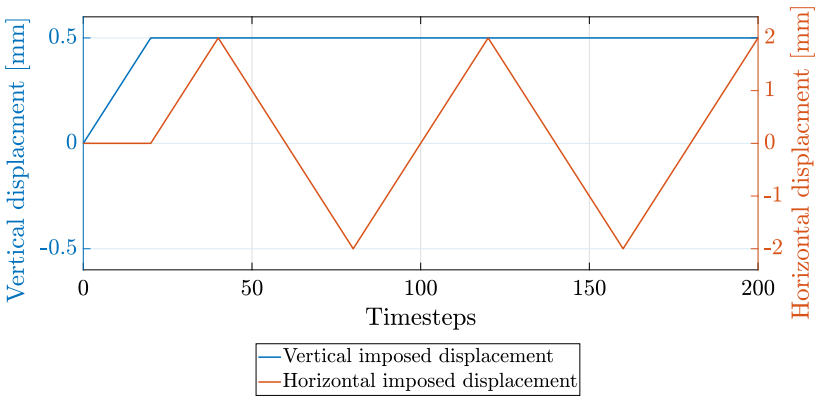

Fig. 13. Normal and tangential displacements imposed to the flat indenter during a simulation under cyclic loading.

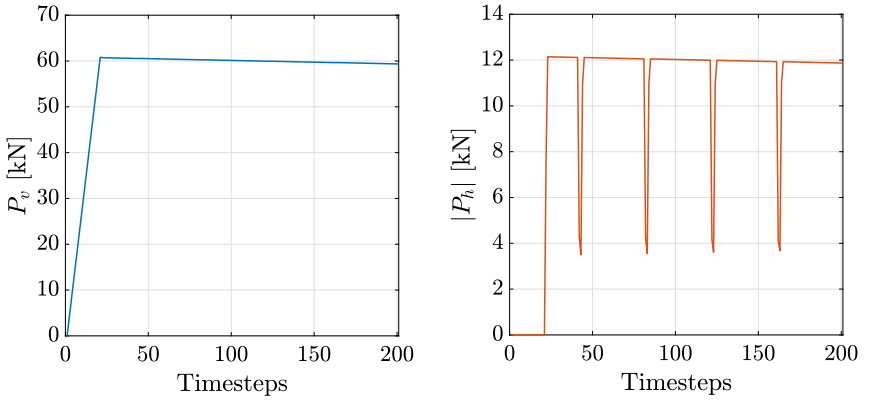

(a) Normal reaction force

(b) Absolute value of the tangential reaction force

Fig. 14. Reaction force evolution for the simulation under cyclic loading.

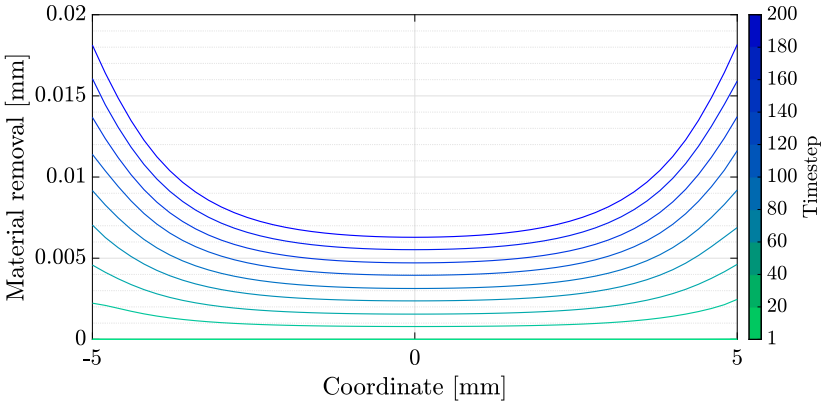

(a) Material removal for during the cyclic simulation

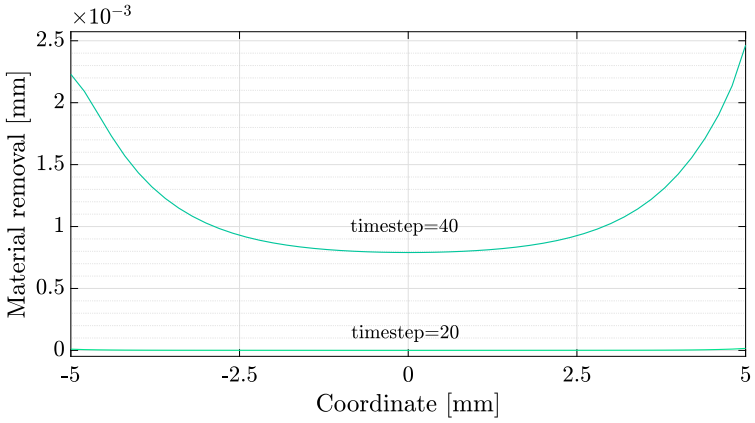

(b) Material removal for (a) overall simulation, and (b) at the instance of $t_s = 20$ corresponding to normal loading phase, and $t_s = 40$ corresponding to first tangential loading phase.

Fig. 15. (a) Material removal for the flat indenter subject to cyclic loading. (b) Detail of the results at $t_s = 20$ (at the end of the normal loading phase) and at $t_s = 40$ (corresponding to $\bar{u}_x = 2$ mm).

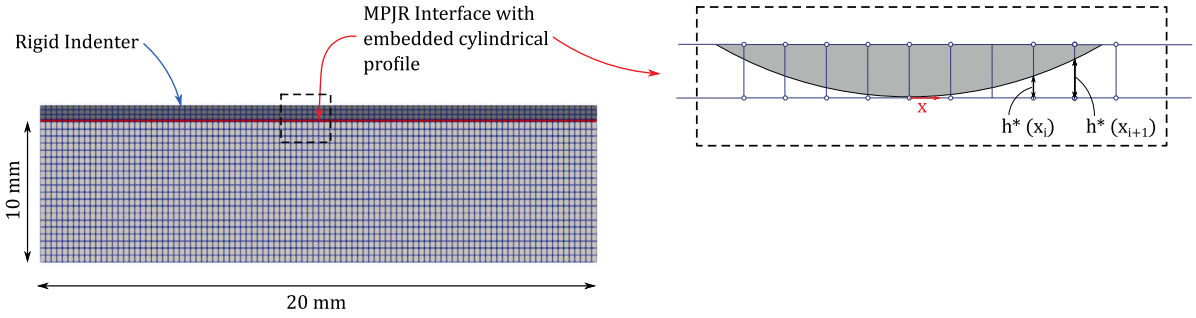

Fig. 16. Geometry and mesh discretization used for the simulation of the cylindrical indenter with radius $R = 10 \div 100$ mm. The real cylindrical geometry is embedded into the FEM model using the MPJR interface finite element which avoid the explicit profile discretization.

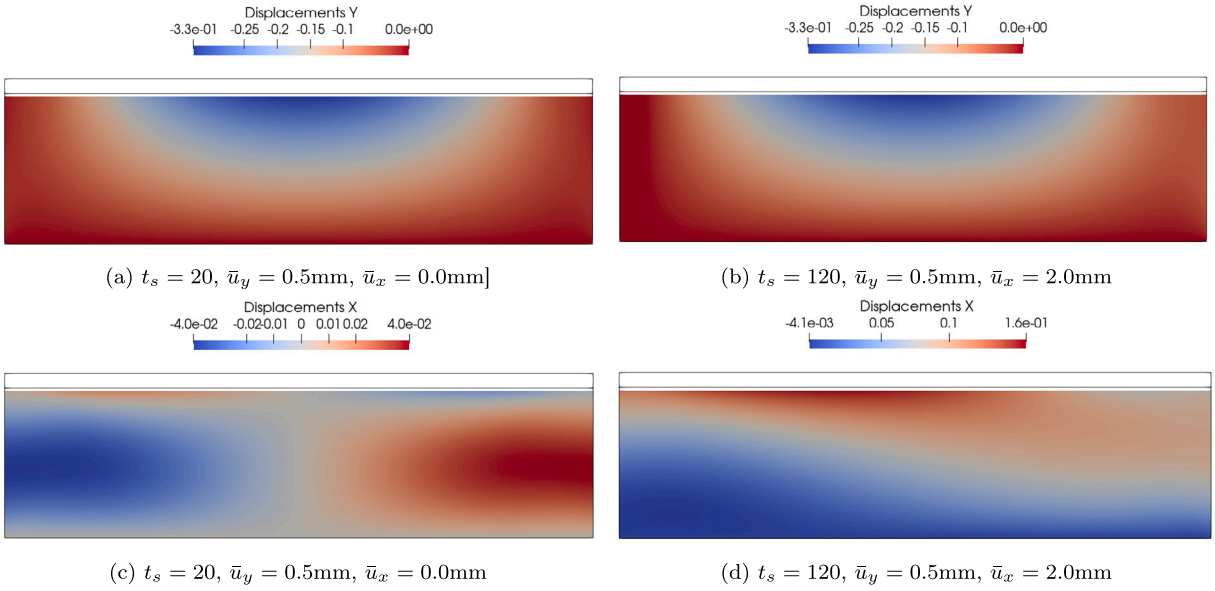

(a) $t_s = 20$, $\bar{u}_y = 0.5$mm, $\bar{u}_x = 0.0$mm] (b) $t_s = 120$, $\bar{u}_y = 0.5$mm, $\bar{u}_x = 2.0$mm

(c) $t_s = 20$, $\bar{u}_y = 0.5$mm, $\bar{u}_x = 0.0$mm (d) $t_s = 120$, $\bar{u}_y = 0.5$mm, $\bar{u}_x = 2.0$mm

Fig. 17. Contour plots of the normal displacements in (a) e (b), and of the tangential displacement in (c) and (d) at different pseudo-time steps t_s.

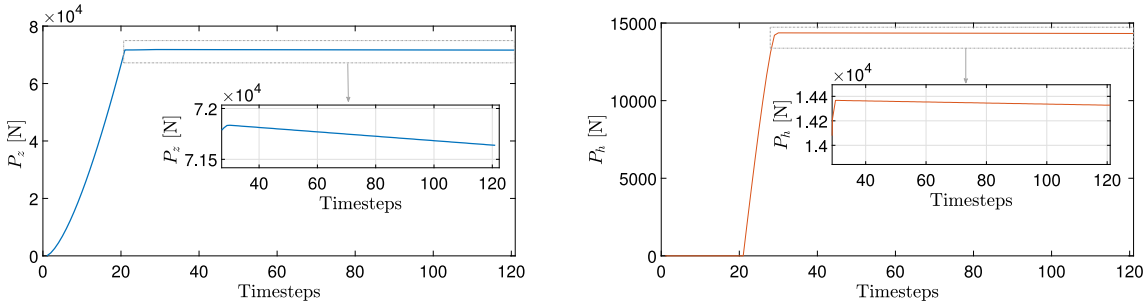

(a) Normal reaction force (b) Tangential reaction force

Fig. 18. Reaction forces for the cylindrical indenter simulations.

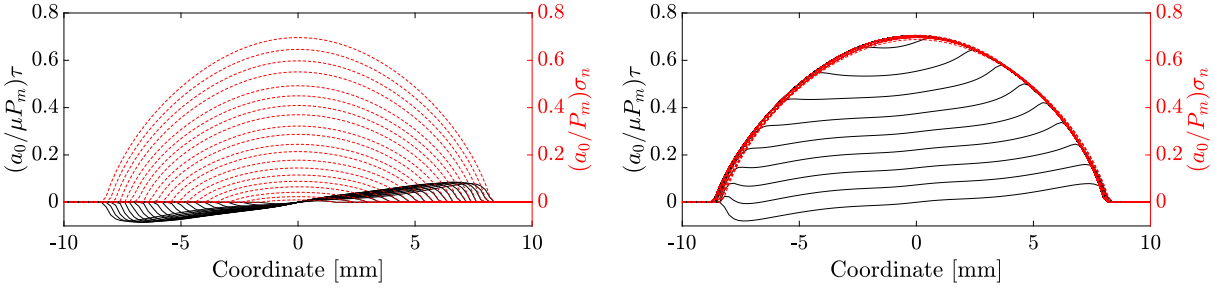

(a) Tractions during the normal loading phase (b) Tractions during the tangential loading phase

Fig. 19. Normal contact tractions (red) and tangential contact tractions (black) during the two loading phases.

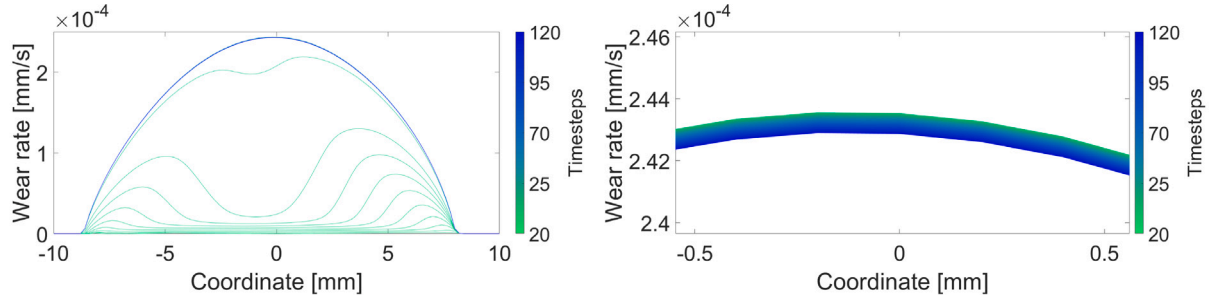

(a) Tangential loading phase (b) Gross sliding phase (detail)

Fig. 20. Wear rate during the tangential loading phase, and then a zoom on the wear rate evolution during the gross sliding stage when the interface undergoes full slip.

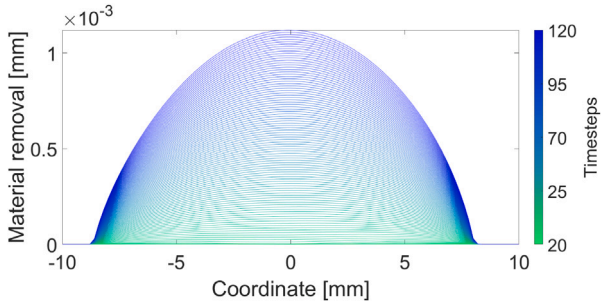

Fig. 21. Detail of the material removal due to wear during the tangential loading phase.

Table 3
Parameters used for the Weierstrass profiles.

Model parameter	Value
D	1.75
n_w	10
γ	5
λ_0	2 mm
g_0	0.1 mm and 0.5 mm

WM profile, $n_w = 10$ is considered with different values of g_0 to simulate rough profiles of different amplitudes.

The geometric description and the discretization employed for the rough profiles are the same used for the cylindrical case, see Fig. 16 and summarized in Table 2. To capture the geometric features of the profile, a mesh consisting of 100 elements along the contact interface is used to discretize the WM profiles.

The evolution of the normal contact pressure during the normal loading phase is shown in Fig. 27. It can be noticed that only the profile with a smaller amplitude g_0 reaches full contact, while the profile with a higher amplitude achieved only partial contact for the same value of $\bar{u}_y$.

The tangential contact tractions are shown in Fig. 28 and present a similar trend for both profiles, showing the transition from full stick to full sliding.

The evolution of wear rate and the material removal from the substrate predicted by the simulations are shown in Figs. 29 and 30. It is interesting to note that, as expected, the model reproduces the material loss only in the contact areas.

To comprehensively understand the effects of roughness, the effect of the number of harmonics on the wear results has been compared. For each chosen value of g_0 analyzed in the previous paragraphs, the value of n_w has been set equal to $10, 5, 1$, decreasing the number of harmonics of the WM profiles. The results at the end of the simulations are compared in terms of wear rate in Fig. 31. For visualization purposes, only one part of the interface has been shown in the plots ($0 \leq x \leq 5$ mm). It can be seen that the wear rate increases with the number of harmonics of the profile, and this effect is more visible for the profiles with $g_0 = 0.5$ mm.

5.4. Effect of the local wear coefficient and insight into the global (emergent) measurable wear coefficient

In the present study, the existence of an Archard wear law applicable at the local scale has been postulated, with a local wear rate coefficient k_w considered as a true material property.

Here, we first remark that a variation of the local wear coefficient between 1×10^{-11} MPa^{-1} to 1×10^{-7} MPa^{-1} leads to a linear shift of the predicted wear rate and material removal profiles, see e.g. Fig. 32 for the flat indenter and Fig. 33 for the smooth cylindrical indenter with $R = 100$ mm, as exemplary cases.

As clearly observable from the above results, the spatial evolution of wear along the interface is strongly affected by the overall indenter geometry, which in turn leads to different nonuniform normal contact traction distributions. This occurs even for the flat indenter if it has a finite size. This poses enormous complexities in decoupling the geometrical effects related to indenter geometry or, for nominally flat surfaces, related to roughness from microscopical effects responsible for wear. This is particularly true if we consider that during the majority of engineering experiments only global quantities can be measured.

With the aid of the present computational framework, one could attempt to identify the local wear coefficient by matching global wear measurements. Using global data one can in fact estimate a global wear coefficient K_w dependent on the material properties and on the profile geometry as follows:

$$K_w = \frac{\Delta_w}{P_v \bar{u}_x} \tag{54}$$

where $\bar{u}_x$ is the sliding distance, equal to 2 mm for all the simulated cases in this work, P_v is the normal force at the end of the contact mechanics simulation conducted all under the same far-field imposed normal displacement, and Δ_w is the total material removal computed by integrating the amount of material removal at the last pseudo-time step $t_s = 120$ of the simulations.

The resulting values of K_w for all the different simulated indenters are compared in Table 4. The global wear coefficients are always higher than the local wear coefficient, and differ for all the cases as a result of the impact of the geometry on the traction distributions.

Therefore, for a given globally measured wear coefficient K_w and profile topography, which can be assessed with accuracy using confocal profilometers, the present computational framework could be exploited by framing the contact simulation as an inverse problem where the local wear coefficient k_w that represents the material property to be identified is determined by minimizing the error between the predicted and measured global wear rate.

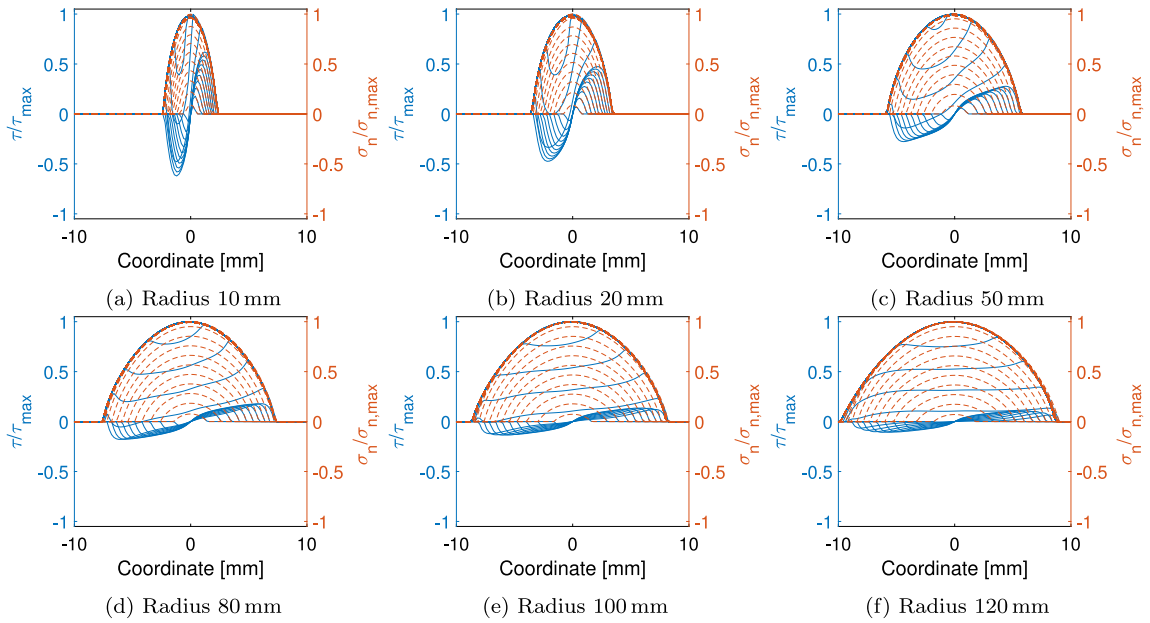

(a) Radius 10 mm (b) Radius 20 mm (c) Radius 50 mm

(d) Radius 80 mm (e) Radius 100 mm (f) Radius 120 mm

Fig. 22. Contact tractions for different radii of the cylindrical indenter.

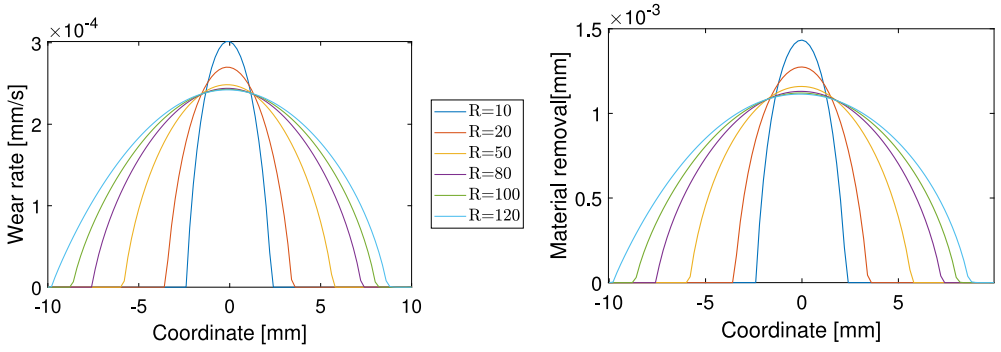

(a) Wear rate (b) Material removal

Fig. 23. Comparison of the wear rate and material removal from the substrate for different indenter radii at the end of the simulation (pseudo-time step 120).

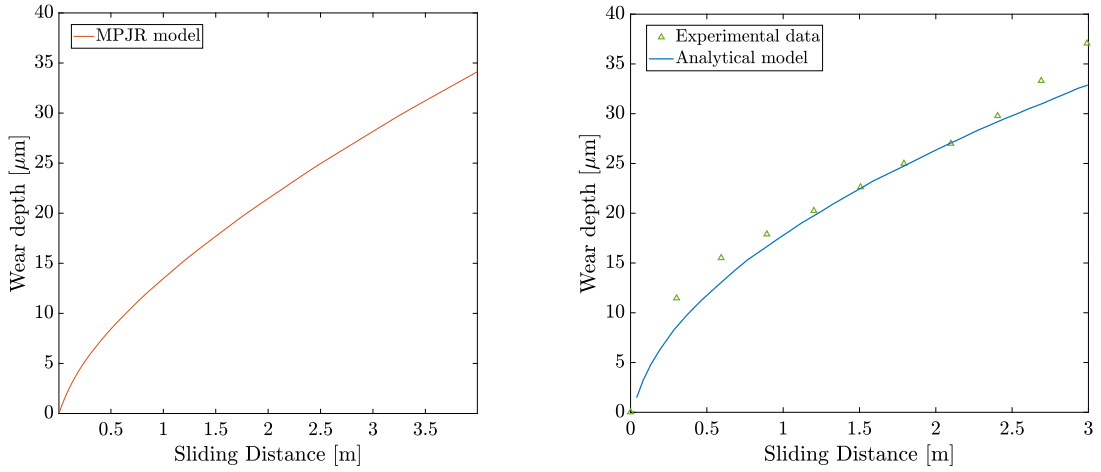

(a) Simulation results of the proposed MPJR computational framework.

(b) Experimental results from [12] and analytical model developed in [8].

Fig. 24. Comparison of the wear depth prediction obtained with the proposed MPJR approach for the case of a cylindrical indenter under harmonic loading (a), and experimental and analytical results for a spherical pin subject to the same loading conditions (b).

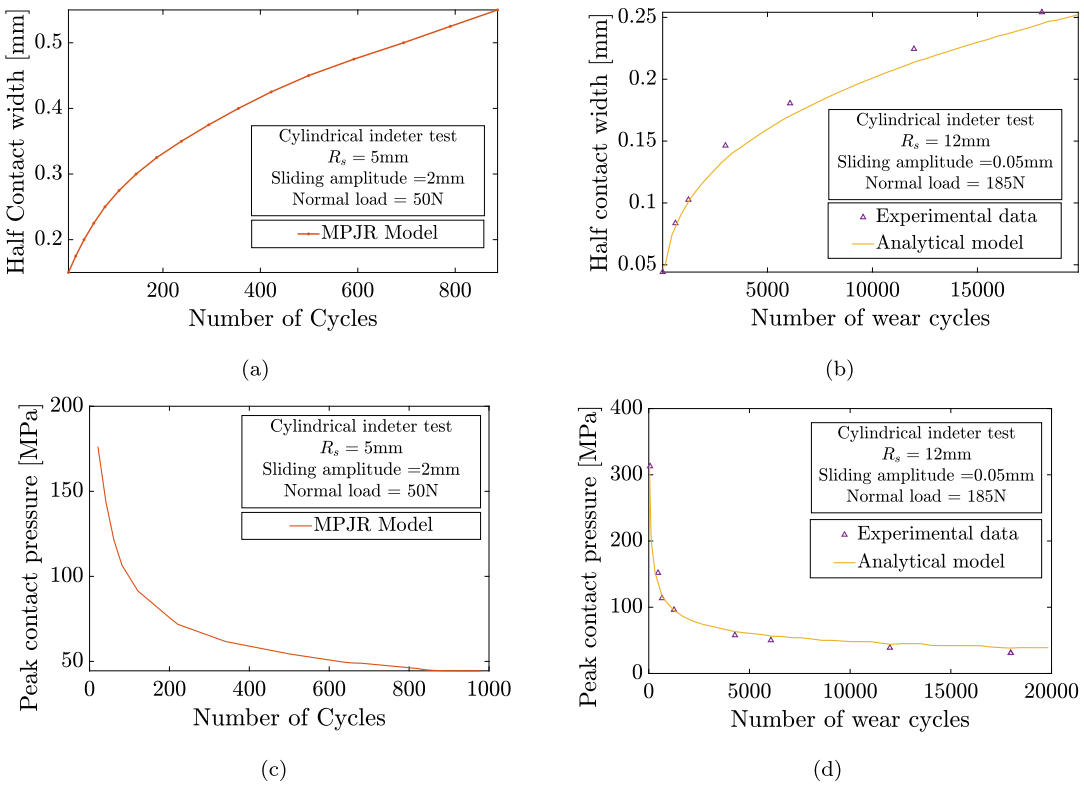

Fig. 25. Comparison of the half contact width and peak contact pressure predictions for the case of a cylindrical indenter under harmonic loading obtained with the proposed MPJR approach (a,c) and experimental [19] and analytical [9] results available in the literature for a similar test (b,d).

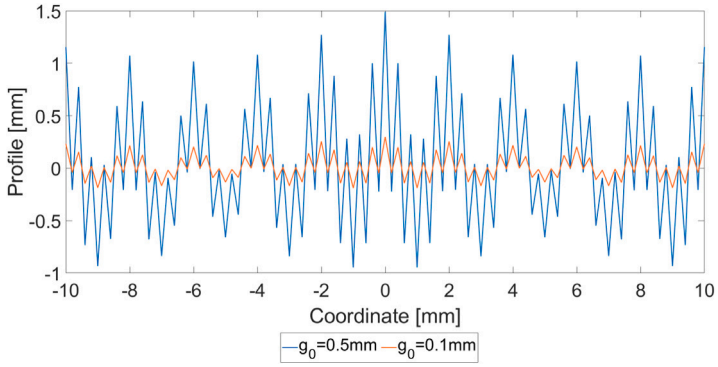

Fig. 26. Simulated Weierstrass rough profiles with different amplitude g_0.

Table 4
Macro-scale wear coefficients.

Indenter geometry	P_v [N]	Local k_w [MPa^{-1}]	Global K_w [MPa^{-1}]
Cylinder (R = 10 mm)	2.55×10^4	1×10^{-7}	9.56×10^{-7}
Cylinder (R = 20 mm)	3.40×10^4	1×10^{-7}	9.51×10^{-7}
Cylinder (R = 50 mm)	5.16×10^4	1×10^{-7}	9.42×10^{-7}
Cylinder (R = 80 mm)	6.45×10^4	1×10^{-7}	9.35×10^{-7}
Cylinder (R = 100 mm)	7.16×10^4	1×10^{-7}	9.31×10^{-7}
Cylinder (R = 120 mm)	7.79×10^4	1×10^{-7}	9.28×10^{-7}
WM (λ_0 = 2 mm, g_0 = 0.1 mm, n_w = 1)	9.28×10^4	1×10^{-7}	9.19×10^{-7}
WM (λ_0 = 2 mm, g_0 = 0.1 mm, n_w = 5)	1.15×10^5	1×10^{-7}	8.99×10^{-7}
WM (λ_0 = 2 mm, g_0 = 0.1 mm, n_w = 10)	1.21×10^5	1×10^{-7}	8.94×10^{-7}
WM (λ_0 = 2 mm, g_0 = 0.5 mm, n_w = 1)	3.17×10^4	1×10^{-7}	9.70×10^{-7}
WM (λ_0 = 2 mm, g_0 = 0.5 mm, n_w = 5)	1.22×10^5	1×10^{-7}	8.86×10^{-7}
WM (λ_0 = 2 mm, g_0 = 0.5 mm, n_w = 10)	1.45×10^5	1×10^{-7}	8.66×10^{-7}

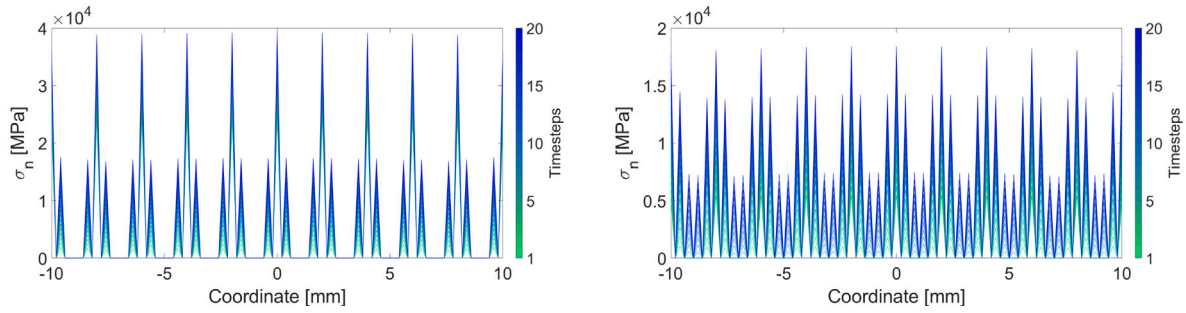

(a) Profile with amplitude $g_0 = 0.5\,\mathrm{mm}$ (b) Profile with amplitude $g_0 = 0.1\,\mathrm{mm}$

Fig. 27. Normal contact tractions during the normal loading phase. The profile with smaller g_0 achieves full contact.

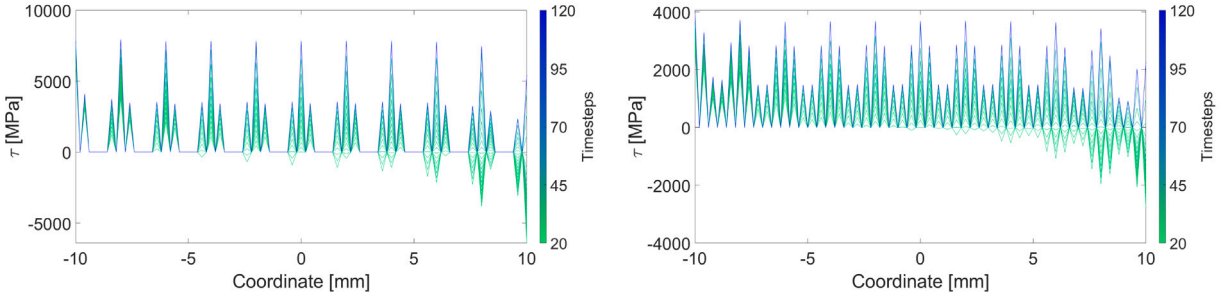

(a) Profile with amplitude $g_0 = 0.5\,\mathrm{mm}$ (b) Profile with amplitude $g_0 = 0.1\,\mathrm{mm}$

Fig. 28. Tangential contact tractions during the increasing tangential loading phase.

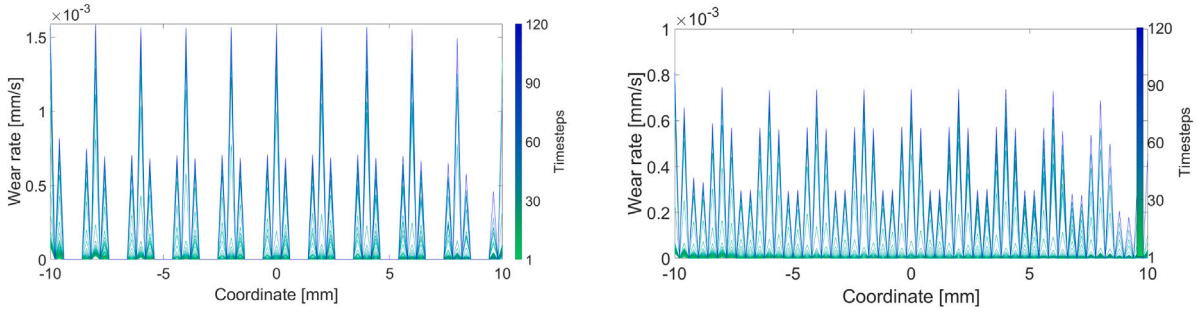

(a) Profile with amplitude $g_0 = 0.5\,\mathrm{mm}$ (b) Profile with amplitude $g_0 = 0.1\,\mathrm{mm}$

Fig. 29. Comparison of the wear rate for the rough profiles.

6. Conclusion

In this work we derived a comprehensive two dimensional variational formulation and finite element discretization for the simulation of wear in frictional contact problems in relation to indenters of any arbitrary shape and with also roughness. The authors implemented the wear model in the finite element software FEAP v.8.6 [67] specifically designed for research purposes.

Standard approaches availables in the literature for FE simulations require the explicit discretization of the indenter geometry, the update of the surface node position due to wear at each timestep and the consequent remeshing of the updated geometry, generating a very expensive computational method. Wear simulations in Abaqus, for

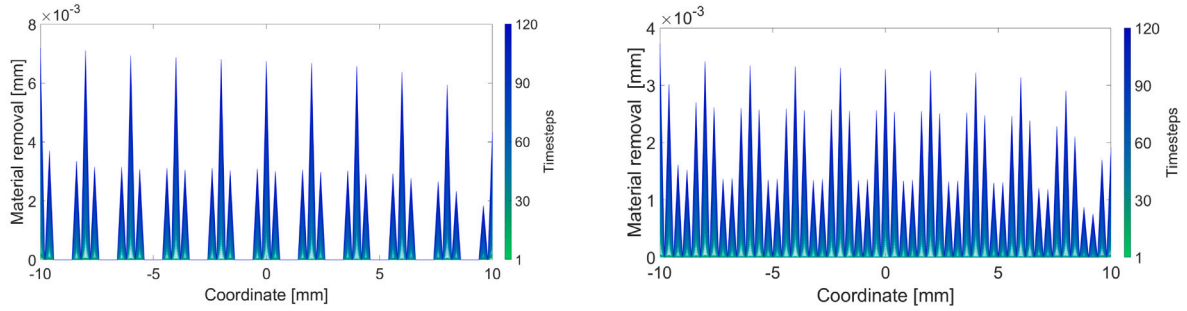

(a) Profile with amplitude $g_0 = 0.5\,\text{mm}$ (b) Profile with amplitude $g_0 = 0.5\,\text{mm}$

Fig. 30. Comparison of the material removal for the rough profiles.

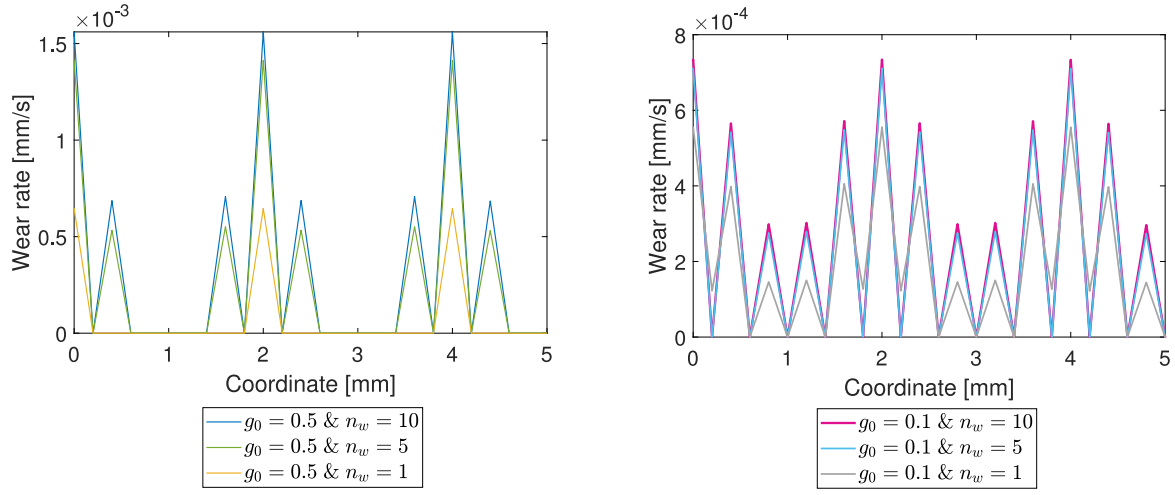

(a) Profile with amplitude $g_0 = 0.5\,\text{mm}$ (b) Profile with amplitude $g_0 = 0.1\,\text{mm}$

Fig. 31. Comparison of the wear rate at the end of the simulations for different rough profiles obtained varying g_0 and the number of harmonics n_w.

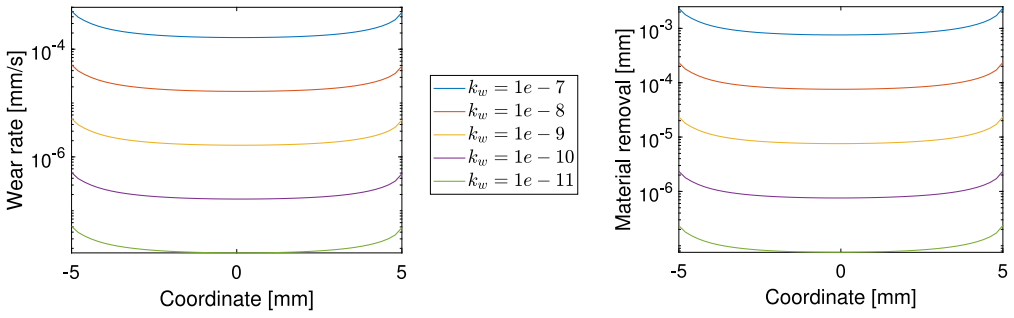

(a) Wear rate (b) Material removal

Fig. 32. Effect of the wear coefficient k_w (unit of measure MPa^{-1}) on the wear rate and on the material removal at the end of the simulation for the flat indenter.

example, are mostly based on the use of the UMESHMOTION subroutine combined with the ALE (Arbitrary-Lagrangian–Eulerian) technique (see the review [68] and the references therein given). The proposed approach avoids the remeshing operations, since wear computation and the surface geometry update at each timestep is directly taken into account inside the MPJR interface finite element routine. This aspect decreases the required computational effort and allows also for the simulation of more complex geometries. It is important to notice that the proposed methodology can be exploited also in Abaqus or other similar FE software coding an equivalent interface finite element (in the case of Abaqus using the UEL subroutine), opening to applications in the industrial sector where Abaqus or other commercial software are commonly employed.

Postulating the existence of a local (microscopical) Archard wear law with a local wear coefficient as a true material property, the proposed computational framework predicts contact tractions, wear rates and material removal along the interface for any complex loading histories, which have been for demonstration purposes limited to normal contact phase followed by a tangential loading phase under constant normal displacement and up to gross sliding. The methodology is of course general and can handle also cyclic loading conditions.

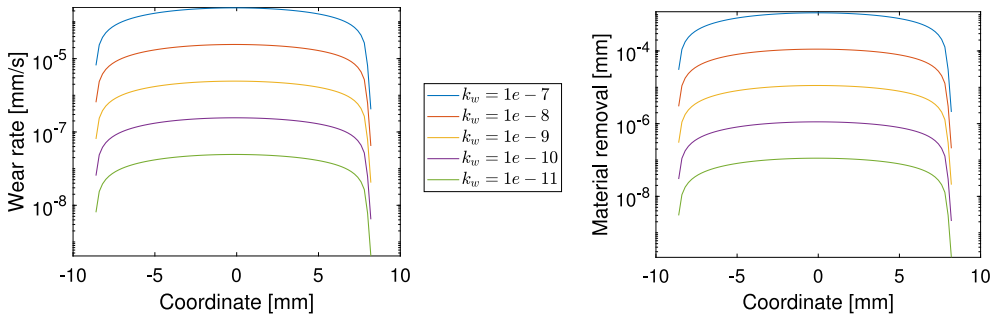

(a) Wear rate (b) Material removal

Fig. 33. Effect of the wear coefficient k_w (unit of measure MPa^{-1}) on the wear rate and on the material removal at the end of the simulation for the cylindrical indenter.

Benchmark tests have included three indenter profiles: flat, cylindrical, and nominally rough according to the Weierstrass–Mandelbrot function. The computational framework has been validated against experimental and analytical models, proving that the proposed approach is capable of reproducing trends typical of Hertzian contacts. Results open new perspectives to correlate the global wear coefficient, that can be measured from global quantities from experiments, and local wear properties intrinsic of the material which are very difficult to be assessed due to the intrinsic coupling between surface geometry (indenters with different smooth shapes or nominally flat but microscopically rough) and the overall evolution of wear.

CRediT authorship contribution statement

Francis John: Writing – original draft, Visualization, Software, Methodology, Formal analysis, Data curation. **Pavan Kumar Asur Vijaya Kumar:** Writing – review & editing, Writing – original draft, Validation, Supervision, Methodology, Investigation, Formal analysis. **Maria Rosaria Marulli:** Writing – review & editing, Writing – original draft, Validation, Supervision, Methodology, Investigation, Formal analysis. **Marco Paggi:** Writing – review & editing, Writing – original draft, Validation, Supervision, Project administration, Formal analysis, Conceptualization.

Declaration of competing interest

The authors declare that they have no known competing financial interests or personal relationships that could have appeared to influence the work reported in this paper.

Acknowledgements

The H2020 Marie Sklodowska-Curie Staff Exchanges project DIAGONAL — Ductility and Fracture Toughness Analysis of Functionally Graded Materials — (GA 101086342) is gratefully acknowledged.

Data availability

Data will be made available on request.

References

[1] Li B, Li P, Zhou R, Feng XQ, Zhou K. Contact mechanics in tribological and contact damage-related problems: A review. Tribol Int 2022;171(March):107534. http://dx.doi.org/10.1016/j.triboint.2022.107534.

[2] Archard JF. Contact and rubbing of flat surfaces. J Appl Phys 1953;24(8):981–8. http://dx.doi.org/10.1063/1.1721448.

[3] Zmitrowicz A. Contact mechanics of wearing out solids. In: Wriggers P, Nackenhorst U, editors. IUTAM symposium on computational methods in contact mechanics. Dordrecht: Springer Netherlands; 2007, p. 311–31.

[4] Carollo V, Paggi M, Reinoso J. The steady-state archard adhesive wear problem revisited based on the phase field approach to fracture. Int J Fract 2019;215(1–2):39–48. http://dx.doi.org/10.1007/s10704-018-0329-0.

[5] Bonari J, Paggi M, Dini D. A new finite element paradigm to solve contact problems with roughness. Int J Solids Struct 2022;111643. http://dx.doi.org/10.1016/j.ijsolstr.2022.111643.

[6] Goryacheva IG. Contact mechanics in tribology. springer Dordrecht; 1998, http://dx.doi.org/10.1007/978-94-015-9048-8.

[7] Hills DA, Paynter RJ, Nowell D. The effect of wear on nucleation of cracks at the edge of an almost complete contact. Wear 2010;268(7–8):900–4. http://dx.doi.org/10.1016/j.wear.2009.12.015.

[8] Argatov II. Asymptotic modeling of reciprocating sliding wear with application to local interwire contact. Wear 2011;271(7–8):1147–55. http://dx.doi.org/10.1016/j.wear.2011.05.028.

[9] Argatov I, Tato W. Asymptotic modeling of reciprocating sliding wear e comparison with finite-element simulations. Eur J Mech A Solids 2012;34:1–11. http://dx.doi.org/10.1016/j.euromechsol.2011.11.008.

[10] Argatov II, Chai YS. Wear contact problem with friction: Steady-state regime and wearing-in period. Int J Solids Struct 2020;194:213–21. http://dx.doi.org/10.1016/j.ijsolstr.2020.02.019.

[11] Zmitrowicz A. Wear patterns and laws of wear – a review. J Theoret Appl Mech 2006;44(2).

[12] Põdra P, Andersson S. Simulating sliding wear with finite element method. Tribol Int 1999;32(2):71–81. http://dx.doi.org/10.1016/S0301-679X(99)00012-2.

[13] Hugnell AB-J, Björklund S, Andersson S. Simulation of the mild wear in a cam-follower contact with follower rotation. Wear 1996;199(2):202–10. http://dx.doi.org/10.1016/0043-1648(96)06920-7.

[14] Szefer G. Contact problems in terms of large deformations. ZAMM - J Appl Math Mech / Z Angew Math Mech 1998;78(8):523–33. http://dx.doi.org/10.1002/(SICI)1521-4001(199808)78:8%3C523::AID-ZAMM523%3E3.0.CO;2-N.

[15] Strömberg N. A newton method for three-dimensional fretting problems. Int J Solids Struct 1999;36(14):2075–90. http://dx.doi.org/10.1016/S0020-7683(98)00080-8.

[16] Agelet de Saracibar C, Chiumenti M. On the numerical modeling of frictional wear phenomena. Comput Methods Appl Mech Engrg 1999;177(3):401–26. http://dx.doi.org/10.1016/S0045-7825(98)00390-9.

[17] Molinari JF, Ortiz M, Radovitzky R, Repetto EA. Finite-element modeling of dry sliding wear in metals. Eng Comput (Swans Wales) 2001;18(3–4):592–609. http://dx.doi.org/10.1108/00368790110407257.

[18] Ko D-C, Kim D-H, Kim B-M. Finite element analysis for the wear of ti–n coated punch in the piercing process. Wear 2002;252(11):859–69. http://dx.doi.org/10.1016/S0043-1648(02)00032-7.

[19] McColl I, Ding J, Leen S. Finite element simulation and experimental validation of fretting wear. Wear 2004;256(11):1114–27. http://dx.doi.org/10.1016/j.wear.2003.07.001.

[20] Telliskivi T. Simulation of wear in a rolling–sliding contact by a semi-winkler model and the archard's wear law. Wear 2004;256(7):817–31. http://dx.doi.org/10.1016/S0043-1648(03)00524-6.

[21] Kim NH, Won D, Burris D, Holtkamp B, Gessel GR, Swanson P, Sawyer WG. Finite element analysis and experiments of metal/metal wear in oscillatory contacts. Wear 2005;258(11):1787–93. http://dx.doi.org/10.1016/j.wear.2004.12.014.

[22] Lu T, Wu X, Wang Y, Shang P, Zhu Z. Finite element analysis and experimental study on fretting wear of different contact surfaces of fir-tree joint. Tribol Int 2025;207:110631. http://dx.doi.org/10.1016/j.triboint.2025.110631.

[23] Stupkiewicz S. An ale formulation for implicit time integration of quasi-steady-state wear problems. Comput Methods Appl Mech Engrg 2013;260:130–42. http://dx.doi.org/10.1016/j.cma.2013.03.023.

[24] Lengiewicz J, Stupkiewicz S. Continuum framework for finite element modelling of finite wear. Comput Methods Appl Mech Eng 205- 2012;208:178–88. http://dx.doi.org/10.1016/j.cma.2010.12.020, special Issue on Advances in Computational Methods in Contact Mechanics.

[25] Farah P, Wall WA, Popp A. An implicit finite wear contact formulation based on dual mortar methods. Internat J Numer Methods Engrg 2017;111(4):325–53. http://dx.doi.org/10.1002/nme.5464.
[26] Glodež S, Ren Z, Flašker J. Simulation of surface pitting due to contact loading, international. J Numer Methods Eng 1998;43(1):33–50. http://dx.doi.org/10.1002/(SICI)1097-0207(19980915)43:1<33::AID-NME410>3.0.CO;2-Z.
[27] Glodež S, Ren Z, Flašker J. Surface fatigue of gear teeth flanks. Comput Struct 1999;73(1):475–83. http://dx.doi.org/10.1016/S0045-7949(98)00251-X.
[28] Rosenfield A. A fracture mechanics approach to wear. Wear 1980;61(1):125–32. http://dx.doi.org/10.1016/0043-1648(80)90117-9.
[29] Sin H-C, Suh NP. Subsurface crack propagation due to surface traction in sliding wear. J Appl Mech 1984;51(2):317–23. http://dx.doi.org/10.1115/1.3167619.
[30] Dubourg M, Chateauminois A, Villechaise B. In situ analysis and modeling of crack initiation and propagation within model fretting contacts using polymer materials. Tribol Int 2003;36(2):109–19. http://dx.doi.org/10.1016/S0301-679X(02)00137-8, fretting Fatigue.
[31] Mulvihill DM, Kartal ME, Nowell D, Hills DA. An elastic–plastic asperity interaction model for sliding friction. Tribol Int 2011;44(12):1679–94. http://dx.doi.org/10.1016/j.triboint.2011.06.018.
[32] Wu X, Zhang F, Xia H, Zhang L, Liu J, Zhang X, Ao X, Luo J. Effects of asperity shapes and normal loads on adhesive wear mechanisms. Tribol Lett 2025;73(2):1–13. http://dx.doi.org/10.1007/S11249-025-01978-1/FIGURES/12.
[33] Aghababaei R, Warner DH, Molinari JF. On the debris-level origins of adhesive wear. Proc Natl Acad Sci USA 2017;114(30):7935–40. http://dx.doi.org/10.1073/pnas.1700904114.
[34] Pham-Ba S, Molinari J-F. Adhesive wear with a coarse-grained discrete element model. Comput Methods Appl Mech Engrg 2022;397:115124. http://dx.doi.org/10.1016/j.cma.2022.115124.
[35] Collet S, Molinari J-F, Brach S. Variational phase-field continuum model uncovers adhesive wear mechanisms in asperity junctions. J Mech Phys Solids 2020;145:104130. http://dx.doi.org/10.1016/j.jmps.2020.104130.
[36] Zhang H, Goltsberg R, Etsion I. Modeling adhesive wear in asperity and rough surface contacts: A review. Materials 2022;15(19). http://dx.doi.org/10.3390/ma15196855.
[37] Strömberg N. Finite element treatment of two-dimensional thermoelastic wear problems. Comput Methods Appl Mech Engrg 1999;177(3):441–55. http://dx.doi.org/10.1016/S0045-7825(98)00392-2, URL https://www.sciencedirect.com/science/article/pii/S0045782598003922.
[38] Zhao J, Vollebregt EA, Oosterlee CW. A fast nonlinear conjugate gradient based method for 3d concentrated frictional contact problems. J Comput Phys 2015;288:86–100. http://dx.doi.org/10.1016/j.jcp.2015.02.016.
[39] Pohrt R, Li Q. Complete boundary element formulation for normal and tangential contact problems. Phys Mesomech 2014;17(4):334–40. http://dx.doi.org/10.1134/S1029959914040109.
[40] Willner K. Fully coupled frictional contact using elastic halfspace theory. J Tribol 2008;130(3):031405. http://dx.doi.org/10.1115/1.2913537.
[41] Serre I, Bonnet M, Pradeilles-Duval R-M. Modelling an abrasive wear experiment by the boundary element method. C R L' Acad Sci - Ser IIB - Mech 2001;329(11):803–8. http://dx.doi.org/10.1016/S1620-7742(01)01402-7.
[42] Sfantos G, Aliabadi M. Wear simulation using an incremental sliding boundary element method. Wear 2006;260(9):1119–28. http://dx.doi.org/10.1016/j.wear.2005.07.020.
[43] Sfantos G, Aliabadi M. A boundary element formulation for three-dimensional sliding wear simulation. Wear 2007;262(5):672–83. http://dx.doi.org/10.1016/j.wear.2006.08.008.
[44] Rodríguez-Tembleque L, Abascal R, Aliabadi MH. Anisotropic wear framework for 3D contact and rolling problems. Comput Methods Appl Mech Eng 2012;241-244:1–19. http://dx.doi.org/10.1016/j.cma.2012.05.025.
[45] Brink T, Frérot L, Molinari JF. A parameter-free mechanistic model of the adhesive wear process of rough surfaces in sliding contact. J Mech Phys Solids 2021;147(2020):104238. http://dx.doi.org/10.1016/j.jmps.2020.104238.
[46] Hyun S, Pei L, Molinari J-F, Robbins MO. Finite-element analysis of contact between elastic self-affine surfaces. Phys Rev E 2004;70:026117. http://dx.doi.org/10.1103/PhysRevE.70.026117.
[47] Pei L, Hyun S, Molinari J, Robbins MO. Finite element modeling of elasto-plastic contact between rough surfaces. J Mech Phys Solids 2005;53(11):2385–409. http://dx.doi.org/10.1016/j.jmps.2005.06.008.
[48] Wriggers P, Reinelt J. Multi-scale approach for frictional contact of elastomers on rough rigid surfaces. Comput Methods Appl Mech Engrg 2009;198(21):1996–2008. http://dx.doi.org/10.1016/j.cma.2008.12.021, advances in Simulation-Based Engineering Sciences – Honoring J. Tinsley Oden.
[49] Vakis AI, Yastrebov VA, Scheibert J, Nicola L, Dini D, Minfray C, Almqvist A, Paggi M, Lee S, Limbert G, Molinari JF, Anciaux G, Aghababaei R, Echeverri Restrepo S, Papangelo A, Cammarata A, Nicolini P, Putignano C, Carbone G, Stupkiewicz S, Lengiewicz J, Costagliola G, Bosia F, Guarino R, Pugno NM, Müser MH, Ciavarella M. Modeling and simulation in tribology across scales: An overview. Tribol Int 2018;125(February):169–99. http://dx.doi.org/10.1016/j.triboint.2018.02.005.
[50] Frérot L, Aghababaei R, Molinari J-F. A mechanistic understanding of the wear coefficient: From single to multiple asperities contact. J Mech Phys Solids 2018;114:172–84. http://dx.doi.org/10.1016/j.jmps.2018.02.015.
[51] Popov VL, Pohrt R. Adhesive wear and particle emission: Numerical approach based on asperity-free formulation of rabinowicz criterion. Friction 2018;6(3):260–73. http://dx.doi.org/10.1007/s40544-018-0236-4.
[52] Paggi M, Reinoso J. A variational approach with embedded roughness for adhesive contact problems. Mech Adv Mater Struct 2020;27(20):1731–47. http://dx.doi.org/10.1080/15376494.2018.1525454.
[53] Bonari J, Paggi M, Reinoso J. A framework for the analysis of fully coupled normal and tangential contact problems with complex interfaces. Finite Elem Anal Des 2021;196:103605. http://dx.doi.org/10.1016/j.finel.2021.103605.
[54] Bonari J, Paggi M. Viscoelastic effects during tangential contact analyzed by a novel finite element approach with embedded interface profiles. Lubricants 2020;8(12):1–15. http://dx.doi.org/10.3390/lubricants8120107.
[55] Marulli M, Bonari J, Reinoso J, Paggi M. A coupled approach to predict cone-cracks in spherical indentation tests with smooth or rough indenters. J Mech Phys Solids 2023;178:105345. http://dx.doi.org/10.1016/j.jmps.2023.105345.
[56] Moore DF. Principles and applications of tribology - 1st edition. Pergamon Int Libr Sci: Int Ser Mater Sci Technol 1975.
[57] Sato Y. Design of rail head profiles with full use of grinding. Wear 1991;144(1):363–72. http://dx.doi.org/10.1016/0043-1648(91)90027-R.
[58] Olofsson U, Telliskivi T, Wear. Plastic deformation and friction of two rail steels—a full-scale test and a laboratory study. Wear 2003;254(1):80–93. http://dx.doi.org/10.1016/S0043-1648(02)00291-0.
[59] Hills DNDA. Mechanics of fretting fatigue. Dordrecht: Kluwer Academic Publishers; 1994.
[60] K AN, Gregory S. Fretting stresses in single crystal superalloy turbine blade attachments. J Tribol 2000;123(2):413–23. http://dx.doi.org/10.1115/1.1308032.
[61] Vingsbo O, Odfalk M, Ning-E Shen. Fretting maps and fretting behavior of some f.c.c. metal alloys. Wear 1990;138(1):153–67. http://dx.doi.org/10.1016/0043-1648(90)90174-9.
[62] J. Kennedy FE, Ling FF. A thermal, thermoelastic, and wear simulation of a high-energy sliding contact problem. J Lubr Technol 1974;96(3):497–505. http://dx.doi.org/10.1115/1.3452024.
[63] Rabinowicz E. Friction and wear of materials. 2nd ed.. Wiley; 1995, doi:978-0-471-83084-9.
[64] Wriggers P, Korelc J, Junker Ph. First order finite element formulations for third medium contact. Comput Mech 2025. http://dx.doi.org/10.1007/s00466-025-02628-y.
[65] Bonari J. Novel interface discretisation methods for contact mechanics (Ph.D. thesis), IMT School for Advanced Studies Lucca; 2021, http://dx.doi.org/10.6092/imtlucca/e-theses/326.
[66] Ciavarella M, Murolo G, Demelio G, Barber JR. Elastic contact stiffness and contact resistance for the weierstrass profile. J Mech Phys Solids 2004;52(6):1247–65. http://dx.doi.org/10.1016/j.jmps.2003.12.002.
[67] Zienkiewicz O, Taylor R, Zhu J. The finite element method: its basis and fundamentals: seventh edition. Ltd: Elsevier; 2013.
[68] Yan L, Guan L, Wang D, Xiang D. Application and prospect of wear simulation based on ABAQUS: A review. Lubricants 2024;12(2). http://dx.doi.org/10.3390/lubricants12020057.